Influence of atmospheric intraseasonal oscillations on seasonal and interannual variability in the upper Indian Ocean

Benét Duncan[1] and Weiqing Han[2]

Received 7 May 2012; revised 14 September 2012; accepted 9 October 2012; published 28 November 2012.

[1] An ocean general circulation model, the Hybrid Coordinate Ocean Model (HYCOM), is used to examine the rectification of atmospheric intraseasonal oscillations (ISOs) on the mean and seasonal-to-interannual sea surface temperature (SST), mixed layer thickness (hm) and upper ocean heat content in the Indian Ocean. Existing studies have shown that ISOs rectify on seasonal and interannual equatorial surface currents and on cross-equatorial transport, suggesting that they may also have important impacts on upper ocean variability. To evaluate these impacts, a hierarchy of HYCOM experiments isolates the ocean response to forcing by atmospheric ISO events. Other experiments isolate the ocean response to a range of intraseasonal forcing fields including shortwave radiation, precipitation, and winds. Results indicate that rectification of ISOs onto seasonal and interannual upper ocean variability does occur, and that it is important in some regions. The regions displaying maximum rectification vary between SST, hm, and upper ocean heat content, and from seasonal to interannual timescales. Strong seasonal SST rectification occurs in the Arabian Sea and in the Bay of Bengal. Because SSTs in the Arabian Sea are already warm (28°C), the ISO-forced seasonal cycle peak of 0.6°C in May can affect convection there. Intraseasonal wind speed and stress have a much larger impact on seasonal and interannual SST, hm, and upper ocean heat content than either intraseasonal shortwave radiation or precipitation. The relative importance of entrainment and turbulent heat flux due to intraseasonal wind speed, and of upwelling, horizontal advection, and vertical mixing due to intraseasonal wind stress, varies with region.

Citation: Duncan, B., and W. Han (2012), Influence of atmospheric intraseasonal oscillations on seasonal and interannual variability in the upper Indian Ocean, *J. Geophys. Res.*, *117*, C11028, doi:10.1029/2012JC008190.

1. Introduction

1.1. Atmospheric Intraseasonal Oscillations and the Indian Ocean

[2] The tropical Indian Ocean (IO) is a region of enhanced atmospheric intraseasonal oscillations (ISOs) with periods ranging from 10 to 90 days [*Lau and Waliser*, 2005]. The climatic importance of ISOs has received increasing attention. This is because ISOs cannot only cause large amplitude atmospheric and oceanic variability at intraseasonal timescales [e.g., *Harrison and Vecchi*, 2001; *Sengupta et al.*, 2001; *Duvel et al.*, 2004; *Saji et al.*, 2006; *Duvel and Vialard*, 2007; *Vialard et al.*, 2008], but they can also affect the mean state and seasonal-to-interannual variability [e.g., *Waliser et al.*, 2003, 2004; *Han et al.*, 2004; *Halkides et al.*, 2007], and thus impact the tropical climate across a range of time scales. A more detailed review of ISO impacts on the IO follows in Sections 1.2 and 1.3. It has been suggested that ISOs can affect the onset [*McPhaden*, 1999] and termination [*Takayabu et al.*, 1999] of the El Nino Southern Oscillation (ENSO), and the termination of the Indian Ocean Dipole (IOD [e.g., *Saji et al.*, 1999; *Webster et al.*, 1999; *Murtugudde et al.*, 2000; *Yu and Rienecker*, 2000]), as during the 1994 IOD event [*Rao and Yamagata*, 2004; *Han et al.*, 2006b].

[3] On 30-90-day timescales, ISOs are dominated by the Madden-Julian Oscillation (MJO [*Madden and Julian*, 1971, 1972, 1994]). On submonthly timescales, ISOs are dominated by convectively coupled Rossby and Kelvin waves, which peak at 10-20-day periods and are also referred to as the Quasi-Biweekly Mode [e.g., *Murakami and Frydrych*, 1974; *Chen and Chen*, 1993; *Kiladis and Wheeler*, 1995; *Numaguti*, 1995; *Wheeler and Kiladis*, 1999; *Chatterjee and Goswami*, 2004, and references therein]. ISOs exhibit significant interannual variability and pronounced seasonality [e.g., *Li and Wang*, 1994; *Wang and Xie*, 1997; *Hendon et al.*, 1999; *Webster et al.*, 2002]. Strong ISO-scale convection and wind occurs in regions where mean sea surface temperature (SST) is high, typically around the 15°S–15°N equatorial region spanning the Intertropical Convergence Zone (ITCZ) during

[1]Gulf of the Farallones National Marine Sanctuary/University Corporation for Atmospheric Research, San Francisco, California, USA.
[2]Department of Atmospheric and Oceanic Science, University of Colorado Boulder, Boulder, Colorado, USA.

Corresponding author: B. Duncan, Gulf of the Farallones National Marine Sanctuary/University Corporation for Atmospheric Research, 991 Marine Dr., San Francisco, CA 94129, USA. (benet.duncan@colorado.edu)

©2012. American Geophysical Union. All Rights Reserved.
0148-0227/12/2012JC008190

the winter monsoon season (November–April) [*Han et al.*, 2007]. During the Asian summer monsoon (May–October), the ITCZ shifts northward, extending from the eastern equatorial IO to the Bay of Bengal (BOB) and eastern Arabian Sea [*Duncan and Han*, 2009]. As a result, the impacts of ISOs on intraseasonal SSTs also have pronounced seasonality that follows this ISO convection and wind-forcing. The largest SST impacts occur in the Thermocline Ridge region [e.g., *Hermes and Reason*, 2008] of the southwest tropical IO during winter, where the ISO convection and winds are strong, the surface mixed layer is thin, and the thermocline is shallow [e.g., *Duvel et al.*, 2004; *Saji et al.*, 2006; *Han et al.*, 2007]. During the summer monsoon season, the largest impacts of ISOs on SSTs shift to the Arabian Sea and the BOB, where ISO convection and winds are strong [*Saji et al.*, 2006; *Duncan and Han*, 2009].

1.2. ISO Impacts on Intraseasonal Indian Ocean Variability

[4] During recent decades, as high-resolution global-scale satellite wind, precipitation, SST, and other data sets have become available, significant advancements have been made in quantifying the impacts of ISOs on the IO. These satellite data products can adequately resolve atmospheric ISOs and thus provide reliable estimates for their impacts on the ocean. Data analyses using in situ measurements and satellite Tropical Rainfall Measuring Mission (TRMM) SST suggest that the amplitude of intraseasonal SST variability often exceeds 1°C, which is comparable to the SST seasonal cycle [e.g., *Harrison and Vecchi*, 2001; *Sengupta et al.*, 2001; *Duvel et al.*, 2004; *Saji et al.*, 2006; *Duvel and Vialard*, 2007; *Vialard et al.*, 2008].

[5] Ocean model experiments have helped to provide insight into the dynamical and thermodynamical air-sea interaction processes that contribute to intraseasonal tropical IO variability induced by atmospheric ISOs. For example, many modeling studies suggest that atmospheric ISOs can impact SSTs through oceanic processes that bring cooler subsurface water to the mixed layer (e.g., upwelling and entrainment), through horizontal advection, and through surface heat fluxes like evaporative cooling [e.g., *Waliser et al.*, 2003, 2004; *Han et al.*, 2006a, 2007; *Vinayachandran and Saji*, 2008; *Duncan and Han*, 2009; *Halkides and Lee*, 2011; *Jayakumar et al.*, 2011]. Another modeling study showed that the response of the barrier layer and mixed layer in the IO to ISO forcing is an important factor in the intraseasonal SST response [*Schiller and Godfrey*, 2003]. The air-sea interaction processes described above are important because they have been associated with MJO initiation and propagation [e.g., *Flatau et al.*, 1997; *Wang and Xie*, 1998; *Waliser et al.*, 1999; *Kemball-Cook and Wang*, 2001; *Kemball-Cook et al.*, 2002; *Wu et al.*, 2002; *Fu et al.*, 2003; *Maloney and Sobel*, 2004; *Zhang et al.*, 2006; *Watterson and Syktus*, 2007; *Marshall et al.*, 2008]. Intraseasonal winds associated with ISOs also cause intraseasonal zonal currents in the equatorial IO [e.g., *Han et al.*, 2001; *Senan et al.*, 2003; *Nagura and McPhaden*, 2012].

1.3. Rectification of ISOs on the Indian Ocean Mean, Seasonal Cycle, and Interannual Variability

[6] ISOs have been shown to be dependent upon the mean background state [e.g., *Inness and Slingo*, 2003; *Zhang and Dong*, 2004]. In addition, ISOs can have upscale rectification onto the mean state and seasonal-to-interannual variability of the upper IO, which can feed back to the atmosphere and thus modulate MJO initiation, amplitude and propagation. In the Pacific Ocean, existing studies demonstrate that the MJO can rectify onto the ENSO cycle due to the nonlinearity of the oceanic system [*Kessler and Kleeman*, 2000; *Waliser et al.*, 2003].

[7] In the IO, analysis and modeling studies suggest that atmospheric ISOs can shape the mean state, seasonal cycle and interannual variability of the upper ocean. By analyzing NCEP-NCAR reanalysis data, *Shinoda and Hendon* [2002] showed that the MJO could impact the mean, seasonal and interannual wind speed and turbulent heat fluxes. Using an ocean general circulation model (OGCM), *Waliser et al.* [2003, 2004] examined the effect of a composite canonical MJO on the IO. Results suggested that the MJO produced a rectified SST over the intraseasonal event mean, indicating that the MJO may affect the seasonal mean state. Using an OGCM and an intermediate ocean model, *Han et al.* [2004] demonstrated that atmospheric ISOs can impact the mean and seasonal-to-interannual variability of zonal surface current and zonal mass (heat) transport in the equatorial IO, due to the nonlinear response of the ocean to intraseasonal atmospheric forcing. *Halkides et al.* [2007] used OGCM experiments to show that ISOs can reinforce the meridional heat transport at the equator (0°N) and 14.5°S by about 30% during some years. The two latitudes correspond to the cross-equatorial cell (CEC) and the southern subtropical cell (SSTC [*Miyama et al.*, 2003; *Schott et al.*, 2004, 2009]). The CEC connects upwelling zones in the north IO to subduction zones in the southeastern IO via a southward, cross-equatorial branch concentrated in the upper 50 m, and northward bulk-flow of cooler thermocline water. The SSTC connects the open ocean upwelling at the Thermocline Ridge region [e.g., *McCreary et al.*, 1993; *Murtugudde and Busalacchi*, 1998; *Xie et al.*, 2002] to subduction in the southern IO. These wind-driven, shallow meridional overturning circulations are crucial for maintaining the IO heat balance.

1.4. Present Work

[8] To date, no studies have used realistic (non-composite) atmospheric ISO forcing to systematically evaluate the rectification of atmospheric ISOs onto the mean, seasonal cycle, and interannual variability of SST, mixed layer thickness (hm), and upper ocean heat content in the IO. The present work will tackle this problem by performing a series of OGCM experiments forced by observed atmospheric fields from 2000 to 2008. We will evaluate the presence and strength of the rectified effects, and the processes by which they occur. Because the MJO and the Quasi-Biweekly Mode are both important ISOs in the IO, we will examine ISOs as a whole without separately assessing these two timescales of intraseasonal variability.

2. Model and Experiments

2.1. The HYbrid Coordinate Ocean Model (HYCOM)

[9] HYCOM is an OGCM that uses pressure, density, and sigma vertical coordinates to optimize the model's representation of oceanic processes in a variety of conditions [*Bleck*, 2002; *Halliwell*, 2004; *Wallcraft et al.*, 2009].

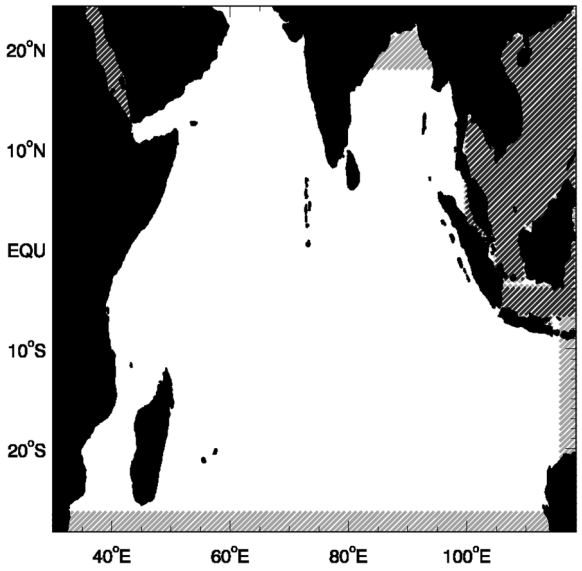

Figure 1. HYCOM model domain. Continents are shaded in solid black and regions removed with a land-sea mask are shaded with black lines. Gray lines indicate regions where model temperature and salinity are relaxed to *Levitus and Boyer* [1994] and to *Levitus et al.* [1994] climatology.

HYCOM has been used in modeling studies of a wide range of regions and ocean basins including the Black Sea, the tropical Pacific Ocean, the Gulf of Mexico, the tropical Atlantic Ocean, and the IO [e.g., *Han et al.*, 2005; *Han et al.*, 2006a, 2006b, 2008; *Kara et al.*, 2005a, 2005b; *Shaji et al.*, 2005; *Prasad and Hogan*, 2007].

[10] Here, HYCOM is configured to the IO basin from 30°S–25°N and 30°E–119°E with horizontal grid spacing of 0.5° × 0.5° and 18 vertical layers. The K-Profile Parameterization [*Large et al.*, 1994, 1997; *Large and Gent*, 1999] is chosen as the vertical mixing scheme and no-slip conditions are applied along continental boundaries. Because this research is focused on the upper ocean response to atmospheric variability, the vertical layers are more closely spaced in the upper ocean than they are in the deep ocean. The Persian Gulf and Red Sea are masked out of the model domain (Figure 1). The effects of the Indonesian Throughflow and BOB rivers are considered by relaxing the temperature and salinity fields in the corresponding regions to *Levitus and Boyer* [1994] and to *Levitus et al.* [1994] climatology. A sponge layer is applied to relax the model solutions to Levitus climatology near the model's southern boundary from 25°S–30°S (Figure 1).

2.2. Forcing Fields

[11] The up-to-date 3-day mean QuickSCAT 10 m neutral winds (www.ssmi.com [*Tang and Liu*, 1996]), National Center for Environmental Prediction (NCEP) surface air temperature and specific humidity, shortwave and longwave fluxes from International Satellite Cloud Climatology Project Flux Data (ISCCP-FD) [*Zhang et al.*, 2004], and Climate Prediction Center Merged Analysis of Precipitation (CMAP) pentad precipitation [*Xie and Arkin*, 1996] are used to force HYCOM from 2000 to 2008. The CMAP pentad precipitation is interpolated to a 3-day interval to match other forcing fields. Note that ISCCP fluxes are available from 2000 to 2006. They are extended to 2008 by regressing NOAA OLR data onto ISCCP fluxes, as in *Duncan and Han* [2009]. In addition, the flux data is tuned by -25 W/m^2 to improve the HYCOM SST simulation (see Section 3.1). This tuning is based on the fact that the mean of the ISCCP fluxes is approximately 25 W/m^2 higher than that of in situ Triangle Trans-Ocean Buoy Network (TRITON) observations (Figure 2a, red dashed line and blue dotted line) [see also *Duncan and Han*, 2009]. QuickSCAT wind stress is calculated from the QuickSCAT 10 m wind vector using the standard bulk formula

$$\vec{\tau} = \rho_a c_d \left|\vec{V}\right| \vec{V}\,, \tag{1}$$

where ρ_a is the density of air (1.175 kg/m^3), c_d is a drag coefficient (0.0013), and $\vec{V}$ is the wind vector. Surface latent and sensible heat fluxes are calculated using the forcing wind, air temperature, and specific humidity data described above, together with HYCOM SST output, in the flux parameterizations of *Kara et al.* [2000].

2.3. Experiments

[12] First, HYCOM is spun up for 30 years using monthly mean climatologies calculated from the forcing fields described above. Then, a series of model experiments is performed from 1 January 2000–31 December 2008 (Table 1). The first experiment, a 'main' run (MR) contains the complete 3-day model forcing fields. In Experiment 1 (EXP1), all of the forcing fields are low-pass filtered to 105 days using a Lanczos filter [*Duchon*, 1979]. Low-pass filtering removes variability shorter than a chosen period, so EXP1 is forced by seasonal and longer timescale atmospheric variability that excludes ISOs. Because the forcing fields are at a 3-day interval, synoptic-scale variability with periods of few days cannot be properly resolved. Therefore, the difference solution MR-EXP1 (Table 2) primarily isolates the ocean's response to atmospheric ISOs.

[13] All of the atmospheric forcing fields are left unfiltered for Experiment 2 (EXP2) with the exception of QuickSCAT wind stress, which is low-pass filtered to 105 days. Similarly, only QuickSCAT wind speed and stress are low-pass filtered to 105 days in Experiment 3 (EXP3). The difference solution MR-EXP2 isolates the ocean's response to intraseasonal wind stress forcing. In HYCOM, wind stress can impact the ocean via Ekman convergence and divergence and horizontal advection. It can also impact mixing because it causes vertical shear in the modeled ocean currents and thus may affect the gradient and bulk Richardson numbers and cause shear instabilities. Difference solutions MR–EXP3 and EXP2-EXP3 isolate the ocean's response to intraseasonal wind in general (wind speed and stress) and wind speed, respectively. HYCOM offers the choice to calculate entrainment through either wind speed or wind stress. We choose the 'wind speed' option, and thus in these HYCOM experiments, wind speed can impact the upper ocean SST via turbulent heat fluxes (THF) and entrainment cooling. Note that THF includes both sensible and latent heat fluxes as calculated by HYCOM using the flux parameterizations of *Kara et al.* [2000]. Entrainment cooling is

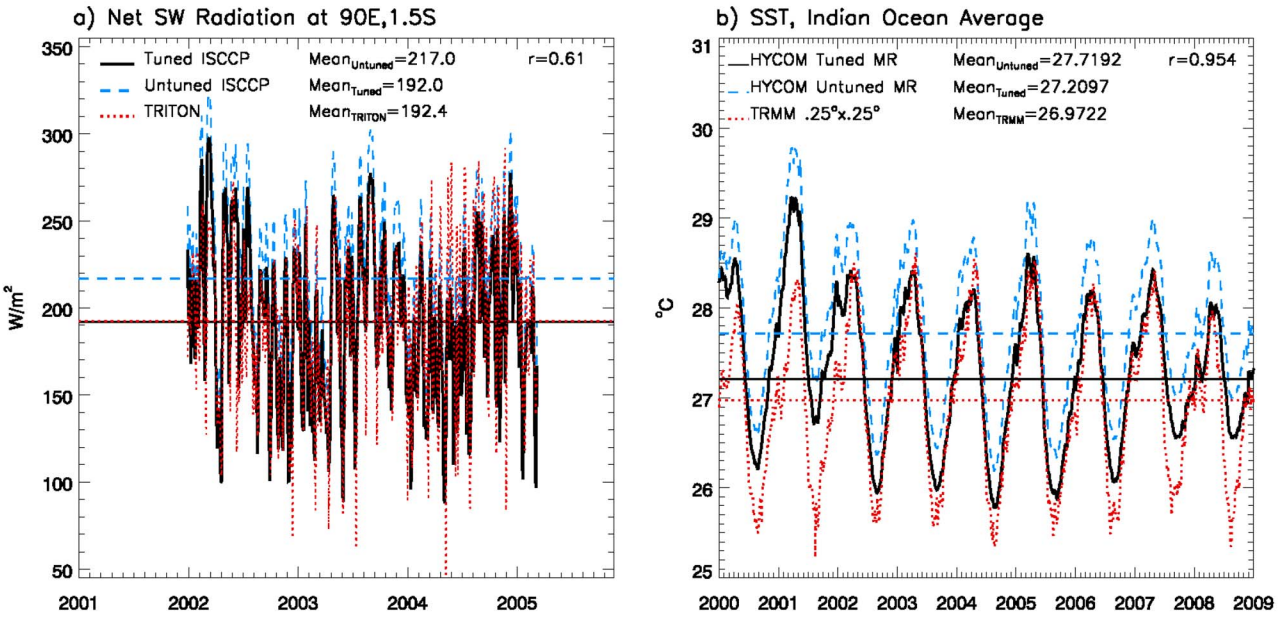

Figure 2. (a) Time series of TRITON (blue dotted line) and ISCCP tuned (black solid line) and untuned (red dashed line) net SW radiation from 21 October 2001 to 4 June 2004 at 90°E, 1.5°S. Horizontal lines show the mean SW radiation from each time series. Because albedo effects are not originally included in the TRITON data, Earth's surface albedo of 3% is applied to it. The tuned ISCCP data is reduced by 25 Wm^{-2}. Standard deviations (STD) and mean values of both ISCCP and TRITON SW radiation are displayed, along with the correlation coefficient (r) between the two. Units are Wm^{-2}. (b) Time series of sea surface temperature (SST) from HYCOM Tuned MR (black solid curve), HYCOM untuned MR (blue dashed curve), and TRMMv4 0.25° × 0.25° (red dotted curve) data, averaged over the whole IO, from 2000 to 2008. Horizontal lines show the mean SST from each time series. The correlation coefficient (r) between HYCOM MR and TRMM SSTs is displayed. Units are °C.

generally calculated from the vertical temperature gradient over a layer and from an entrainment velocity, which is in turn dependent on the vertical velocity at a depth h and on the total time derivative of h [*Stevenson and Niiler*, 1983]. For the surface mixed layer, the total time derivative of h (which includes the effects of horizontal advection on h) is dependent on the upwelling velocity at a depth h and on the entrainment rate [*Stevenson and Niiler*, 1983]. In difference solution EXP2-EXP3, the model response to any forcing fields except for wind speed are removed. Because the upwelling velocity and currents associated with horizontal advection are functions of wind stress, they are approximately the same in both EXP2 and EXP3, and the difference solution removes these effects. Then, entrainment is primarily determined by the local time derivative of h. In this work, the term 'entrainment' is meant to describe the effects of the turbulent frictional velocity (u*; calculated from wind speed) and stratification changes due to THF on the temperature of the mixed layer. Experiments 4 and 5 (EXP4 and EXP5) are forced with low-pass 105 day filtered shortwave (SW) radiation and precipitation, respectively. The difference solutions MR-EXP4 and MR-EXP5 isolate the ocean's response to intraseasonal SW radiation and precipitation.

[14] Note that this approach assumes that the ocean's responses to different forcing fields do not interact. In reality, they may interact due to nonlinearities in the system, thus the sum of oceanic responses to individual forcing fields may not exactly match the response to the total forcing fields. These nonlinear effects are generally small except in some specific regions of the IO where their effects can be significant [e.g., *Han et al.*, 2007; *Duncan and Han*, 2009] (see also Section 3.4). This indicates that the approach of separating the forcing (and thus the associated processes) is

Table 1. Hybrid Coordinate Ocean Model Experiments and Forcings Used[a]

Experiment Number	Forcings Used
MR	All 3-day mean fields: winds, air temperature, humidity, fluxes, precipitation
EXP1	Low-passed (removed less than) 105 days
EXP2	Low-passed wind stress
EXP3	Low-passed wind stress and speed
EXP4	Low-passed shortwave flux
EXP5	Low-passed precipitation
HYCOM_InternalEXP	ERA-Interim monthly climatology

[a]Low-pass frequency is 105 days.

Table 2. Model Experiment Difference Solutions

Difference Solution	Isolates Ocean Response to
MR-EXP1	Atmospheric Intraseasonal Oscillations (ISOs)
MR-EXP2	ISO wind stress
MR-EXP3	ISO wind stress and speed
EXP2-EXP3	ISO wind speed
MR-EXP4	ISO shortwave flux
MR-EXP5	ISO precipitation

generally valid except for some specific regions. Note also that the low-pass filtered wind stress and wind speed include the seasonal-to-interannual components directly rectified by the intraseasonal variability of winds associated with the ISOs [*Shinoda and Hendon*, 2002]. Consequently, this paper focuses on assessing the rectified effects which are caused by the nonlinear response of the upper IO to ISO forcing. THF may contain a rectified component because the bulk formulae used in its calculation are associated with the products of wind speed, air temperature, SST, specific humidity and the wind speed dependent coefficient of *Kara et al.* [2000].

[15] In addition to the ISO rectification effects described above, oceanic internal variability due to nonlinearities in ocean circulation can also affect the modeled seasonal cycle and interannual variability. To assess the effect of this internal variability on the modeled seasonal and interannual signals, an additional HYCOM experiment is performed (HYCOM_InternalEXP; Table 1). HYCOM_InternalEXP is a finer resolution model run, with $0.25^\circ \times 0.25^\circ$ grid spacing and 30 layers [*Wang et al.*, 2012], and it is forced by ERA-Interim monthly climatology [*Dee et al.*, 2011] and run forward in time for 59 years. The results from years 16–40 are analyzed. Because interannual variability does not exist in the model forcing fields in HYCOM_InternalEXP, any interannual variability in the results is due to oceanic internal variability, not ISO rectification.

3. Results

3.1. Model-Data SST Comparison

[16] Averaged over the entire IO, SST variability from HYCOM MR agrees with that from the Tropical Rainfall Measuring Mission v4 (TRMM) data from 2002 to 2008 (Figure 2b), with a correlation coefficient of 0.95 between the two data sets. The discrepancy between HYCOM MR SST and TRMM SST in 2000 and 2001 is primarily due to the model's adjustment from the monthly spin-up forcing to the 3-day mean forcing fields used in the experiments. Consequently, only the years 2002–2008 are analyzed. Without flux tuning, the whole-IO mean of HYCOM SST is $\sim$0.75°C warmer than that of TRMM SST (Figure 2b, blue dashed and red dotted horizontal lines). Reducing ISCCP flux by 25 W/m^2 (Section 2.2 and Figure 2a) improves the simulated HYCOM SST (Figure 2b, black solid and red dotted curves), and the basin mean warm bias decreases to 0.24°C. As a result, all HYCOM experiments listed in Table 1 use ISCCP-FD data that has been corrected by -25 W/m^2.

[17] Monthly climatologies of HYCOM MR and TRMM SSTs, averaged over boreal summer (JJA) and winter (DJF) monsoon months from 2002 to 2008, show that the spatial pattern of the modeled mean seasonal cycle is also consistent with observations (Figure 3). However, the modeled SSTs are warmer than the observed SSTs in most regions of the IO, except in the Thermocline Ridge region (50°E–80°E, 5°S–12°S) where the modeled SSTs are colder than observed. These high modeled SSTs produce the warm basin-mean bias in Figure 2b and in many regions, including the western coasts of Figure 3. One possible reason for the HYCOM warm bias - even after the ISCCP heat flux correction - is that HYCOM's mixed layer is thicker than the mixed layer estimated from World Ocean Atlas data [*Boyer et al.*, 2009] in most regions, but thinner in the Thermocline Ridge region (Figure 4) [see also *Han et al.*, 2007; *Duncan and Han*, 2009]. When the modeled hm is thicker, the monsoon winds cannot cool the upper ocean as quickly as observed. When the mixed layer is thinner, such as in the Thermocline Ridge region, the upper ocean is cooled more quickly, and thus the modeled SST is lower than observed (Figures 3 and 4). In addition, TRMM SST represents skin temperature, whereas HYCOM SST represents the temperature of the near-surface layer with a minimum depth of 3 m. This difference may also contribute to the stronger cooling in TRMM data forced by monsoon winds.

[18] To further quantify the model-data SST comparison, Figure 5 shows time series of the SST seasonal cycle and interannual variability from TRMM, HYCOM MR and EXP1, averaged over regions where ISO impacts are large. See Sections 3.3 and 3.4 for a detailed discussion of the calculation of the seasonal cycle and the selection of these regions. The amplitude of the observed seasonal cycles (Figures 5a and 5b, red dotted lines) is somewhat larger than the modeled seasonal cycles (Figures 5a and 5b, solid black lines), but the timing of the two seasonal cycles is consistent. Removing ISOs from the forcing fields increases the difference between the observed and modeled SST seasonal cycle in the Arabian Sea during April and May (Figure 5a, blue dashed and red dotted curves). In the southwest IO from 10°S–15°S, however, ISO forcing appears to worsen the model/data SST comparison (Figure 5b). That is, ISOs appear to improve the modeled SSTs in the Arabian Sea, and they appear to worsen the modeled SSTs in the southwest IO. As will be discussed in Section 3.4.3, this ISO cooling effect in the southwest IO is likely real, even though it worsens the model/data comparison.

[19] Similar time series of region-averaged HYCOM MR and TRMM SST interannual variability are shown in Figures 5c and 5d. Details about the calculation of interannual variability can be found in Section 3.5. The modeled (solid black line) and TRMM observed (dotted red line) SST interannual variability are fairly consistent in the west equatorial IO and the central IO (Figures 5c and 5d), although the amplitude of the observed interannual variability is often larger than, and sometimes out of phase with, the modeled variability. Correlation coefficients between HYCOM MR and TRMM SSTs are 0.53 and 0.49 in the west equatorial IO and the central IO, respectively.

3.2. ISO Impact on Time Mean Upper-Ocean Variables

[20] Maps of the ISO-forced change in the mean SST, hm, upper ocean heat content, and mixed layer heat content from 2002 to 2008, show that ISO impacts on the mean are regionally dependent, and that these impacts are statistically significant in a large portion of the IO (Figure 6). Heat content over a vertical layer is calculated using the standard formula

$$H = \rho(z) c_p T(z) Z, \tag{2}$$

where $\rho(z)$ is the density of seawater in the layer, c_p is the specific heat of seawater (4.0×10^3 J/kgC), $T(z)$ is the temperature of the layer, and Z is the layer thickness. For upper ocean heat content, Z is 200 m, and $T(z)$ and $\rho(z)$ are

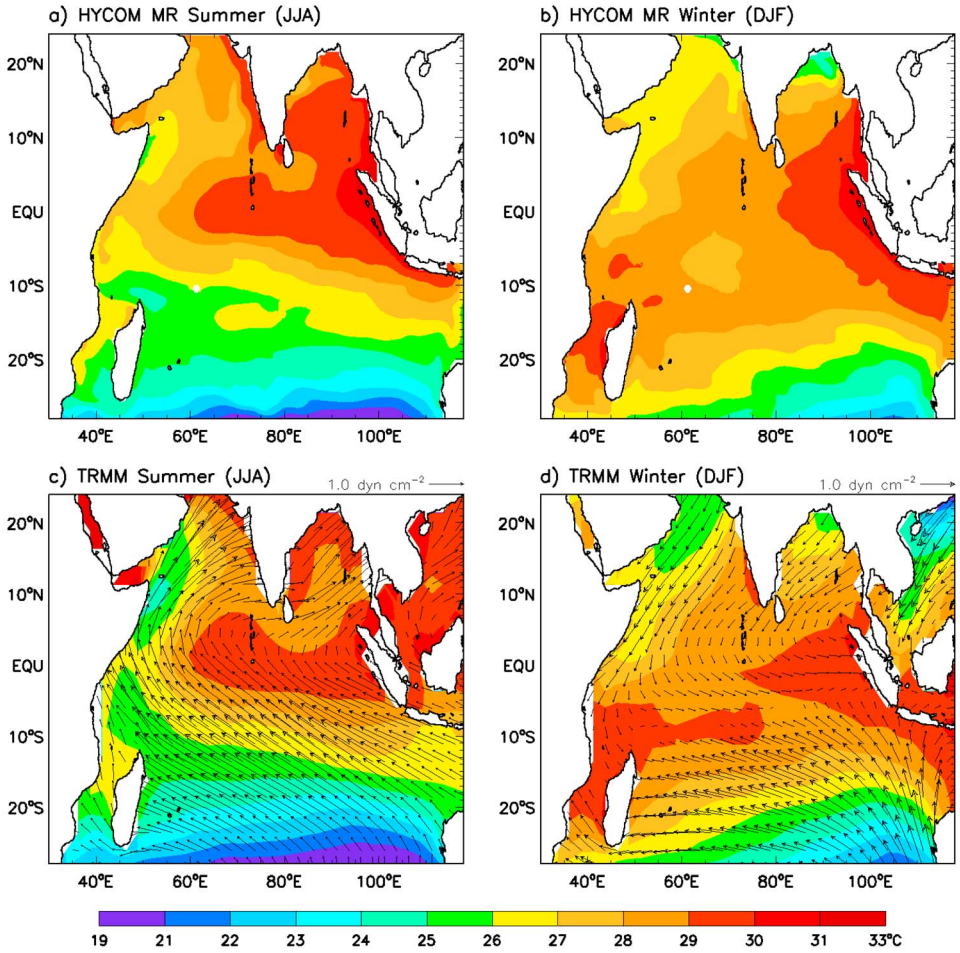

Figure 3. (a) Summertime (June–August) mean SST from HYCOM MR, calculated from monthly mean climatologies. (b) Wintertime (December–February) mean SST from HYCOM MR, calculated from monthly mean climatologies. (c) Same as Figure 3a but from TRMMv4 2.5° × 2.5° SST and with summertime mean QuickSCAT wind vectors overlaid. (d) Same as Figure 3b but from TRMMv4 2.5° × 2.5° SST and with wintertime mean QuickSCAT wind vectors overlaid. Units are °C, ms^{-1}for wind speed, and dyn cm^{-2} for wind stress.

weighted averages over the layer. For mixed layer heat content, Z is the mixed layer thickness, and $T(z)$ and $\rho(z)$ are the mixed layer temperature and density, respectively.

[21] ISOs tend to reduce the mean SST in the equatorial and south IO, but they warm the mean SST in the Arabian Sea and the BOB by 0.1–0.2°C (Figure 6a). The strongest ISO impact on the mean SST occurs along the Sumatran coastline, where SSTs are reduced by 0.1–0.9°C, and along the western coastline of Madagascar, where SSTs are reduced by 0.1–0.5°C. In comparison with the seasonal cycle, which can have an amplitude of over 1°C (Figure 5), these values can be non-negligible in some specific areas. A wide stretch of weaker cooling (0.1–0.3°C) extends between the two regions.

[22] Along the coast of Sumatra and west of Java, the maximum ISO-forced mean hm is 3–12 m (Figure 6b), consistent with the cool SST there (Figure 6a). This thicker hm, together with the cool SST, suggests that anomalous entrainment and upwelling cooling due to ISOs contribute to the pattern of mean cooling there. Different from SST, there is an ISO-forced shallow mean hm anomaly just to the west of the maximum, with hm shoaling by 3–13 m. In the Arabian Sea, mean hm shoals by 3–10 m (deepens by 3–12 m) in the northwest (southeast). Patchy regions of thickened mean hm also stretch across the basin from approximately 15°S–25°S. In these regions, rectification of ISOs onto the mean surface heat fluxes, horizontal advection, and instabilities may play an important role in causing the mean SST change (see Section 3.4.1 for an additional discussion of processes).

[23] The most apparent impacts of atmospheric ISOs on the mean upper ocean (above 200 m) heat content are that they increase the heat content in most regions of the north IO, including the BOB, by up to 3×10^6 Jm^{-2} (Figure 6c). In most regions of the south IO, however, ISOs reduce upper ocean heat content by up to 2×10^6 Jm^{-2}. These results are reminiscent of existing studies on the effects of tropical cyclones, which suggest that tropical cyclones can pump heat into the tropical ocean and affect the meridional heat transport [e.g., *Emanuel*, 2001; *Sriver and Huber*, 2007]. Where does the pumped heat in the north IO eventually go? ISOs cause negative mean upper ocean heat content in the

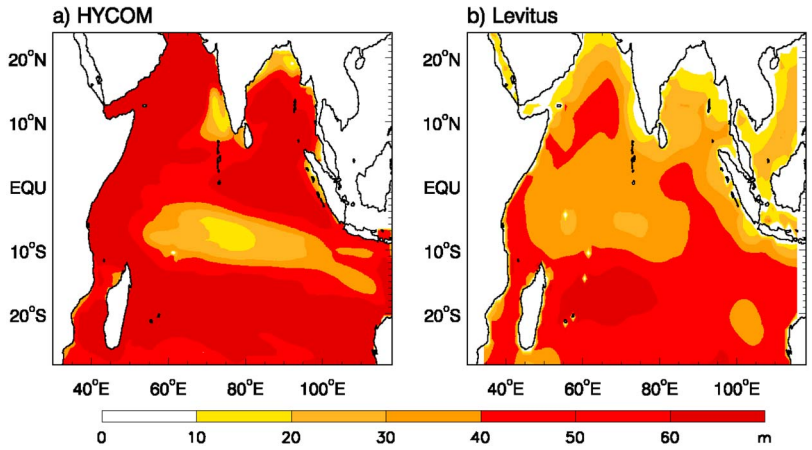

Figure 4. (a) Mean hm from HYCOM MR, calculated from 3-day model output. (b) Mean hm, calculated from monthly mean Levitus WOA09 data. Units are m.

southern IO (Figure 6c), indicating that this north IO heat could be transported to the south by the cross-equatorial cell [*Schott et al.*, 2009], where it is lost by the ocean to the atmosphere. Detailed examination of these processes, however, is beyond the scope of this research.

[24] The pattern of ISO-altered mean mixed layer heat content closely resembles that of hm (Figures 6b and 6d). In some regions like the Sumatra coast, the mean mixed layer heat content increases with the thickening mean hm, even though the mean SST cools there. This suggests that

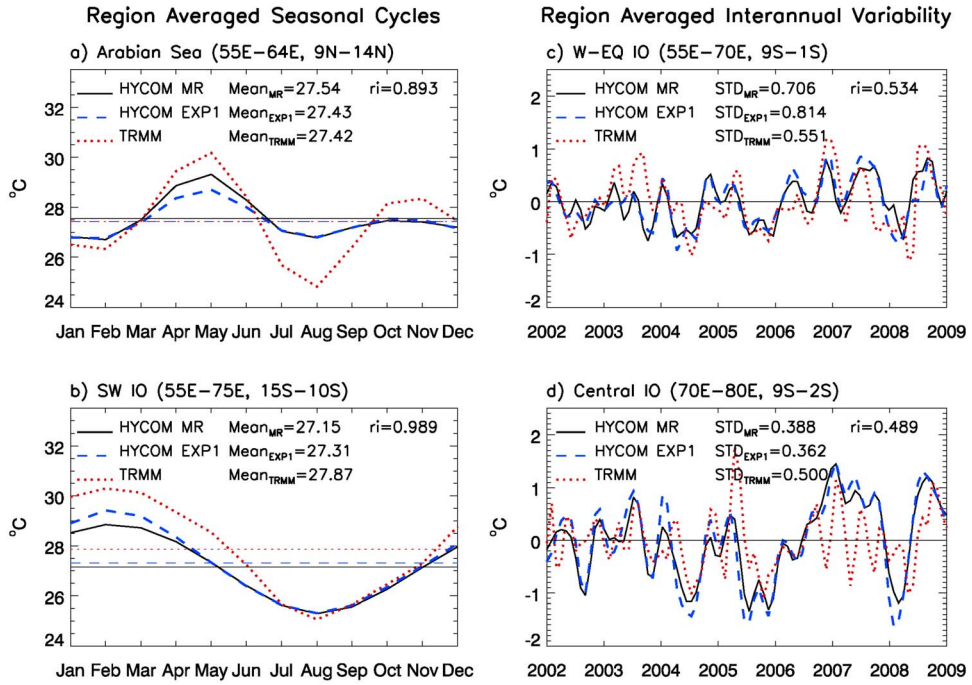

Figure 5. (a) Time series of seasonal SST from 2002 to 2008, averaged over the Arabian Sea (Region 1 in Figure 8c). The black solid, blue dashed, and red dotted curves represent the SST from HYCOM MR, HYCOM EXP1, and TRMMv4 2.5° × 2.5° data. Horizontal lines represent the mean SSTs, which are also calculated and displayed. Differences between HYCOM MR and EXP1 represent the contributions of atmospheric intraseasonal oscillations (ISOs) to the seasonal SST. (b) Same as Figure 5a except averaged over the southwest IO (Region 3 in Figure 8c). (c) Same as Figure 5a except interannual SSTs averaged over the west equatorial IO (Region 1 in Figure 15c). Because mean interannual SSTs are always zero, the horizontal black line represents zero. STDs of SSTs and correlation coefficients (ri) between HYCOM MR and TRMM SSTs are calculated and displayed. (d) Same as Figure 5c except averaged over the central IO (Region 2 in Figure 15c). Units are °C.

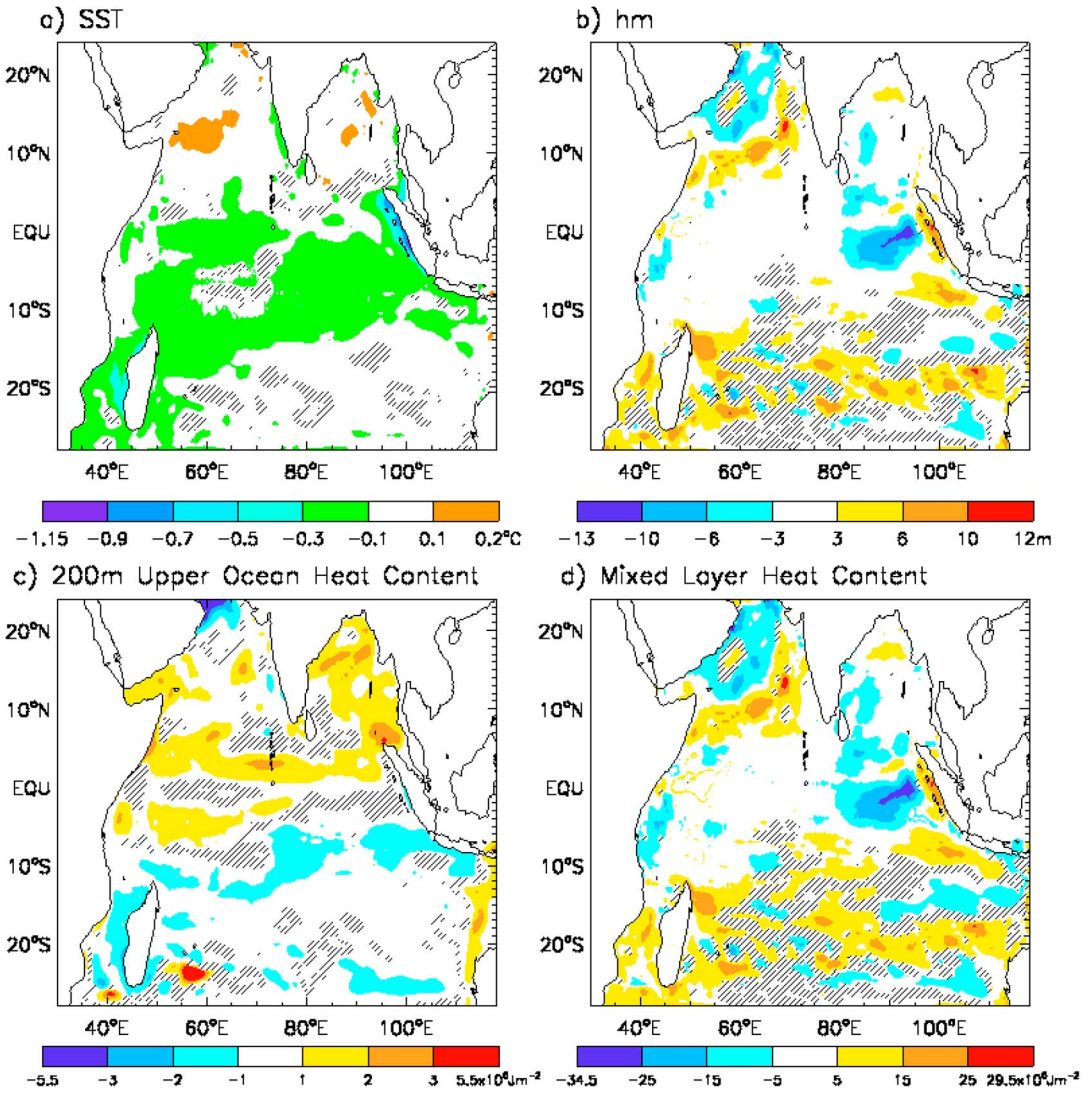

Figure 6. Change in mean HYCOM (a) SST, (b) mixed layer thickness (hm), (c) upper ocean (200 m) heat content, and (d) mixed layer heat content due to ISOs, calculated from mean values of HYCOM MR and EXP1. Calculations of heat content are detailed in Section 3.2. Units are °C for SST, m for hm, and 10^6 Jm^{-2} for heat content. Regions where the change in the mean does not exceed the 95% confidence interval are shaded with diagonal lines.

hm has a much larger impact in determining the mixed layer heat content than SST does. In general, when the ISO-forced SST is warming, the mixed layer is shoaling, indicating reduced entrainment. A thinner mixed layer tends to override the impact of warmer SSTs, resulting in decreased mixed layer heat content.

3.3. ISO Rectification on Seasonal-to-Interannual Variability

[25] Atmospheric ISOs can impact both the mean state and the variability of the upper IO. In order to evaluate the effects of atmospheric ISOs on seasonal-to-interannual ocean variability, we first calculate the monthly averages of low-pass 105 day filtered SST and hm from the 3-day HYCOM difference solution MR-EXP1. Monthly averaging removes the intraseasonal ocean response while preserving the longer timescale seasonal-to-interannual response, and low-pass filtering the data to 105 days before the averaging ensures that the intraseasonal response is fully removed.

[26] The standard deviation (STD) of this monthly averaged ISO-forced SST, hm, upper ocean heat content, and mixed layer heat content provides a basin-wide view of the seasonal-to-interannual IO response to atmospheric ISOs (Figure 7). Similar to the impacts of ISOs on the mean state, the strongest ISO rectification onto SST variability occurs in the south tropical IO, along the west coasts of Sumatra and Madagascar (0.2–0.6°C), and to a lesser degree, in the Arabian Sea and the BOB (0.2–0.4°C) (Figure 7a). ISO-forced upper ocean heat content variability occurs in most regions of the IO north of 15°S, and in a band near 23°S that stretches from the western boundary to 95°E with values ranging from 0.1 to 1.1 × 10^7 Jm^{-2} (Figure 7c). Rectified hm and mixed layer heat content variability have maxima extending south from the Arabian Sea to Madagascar

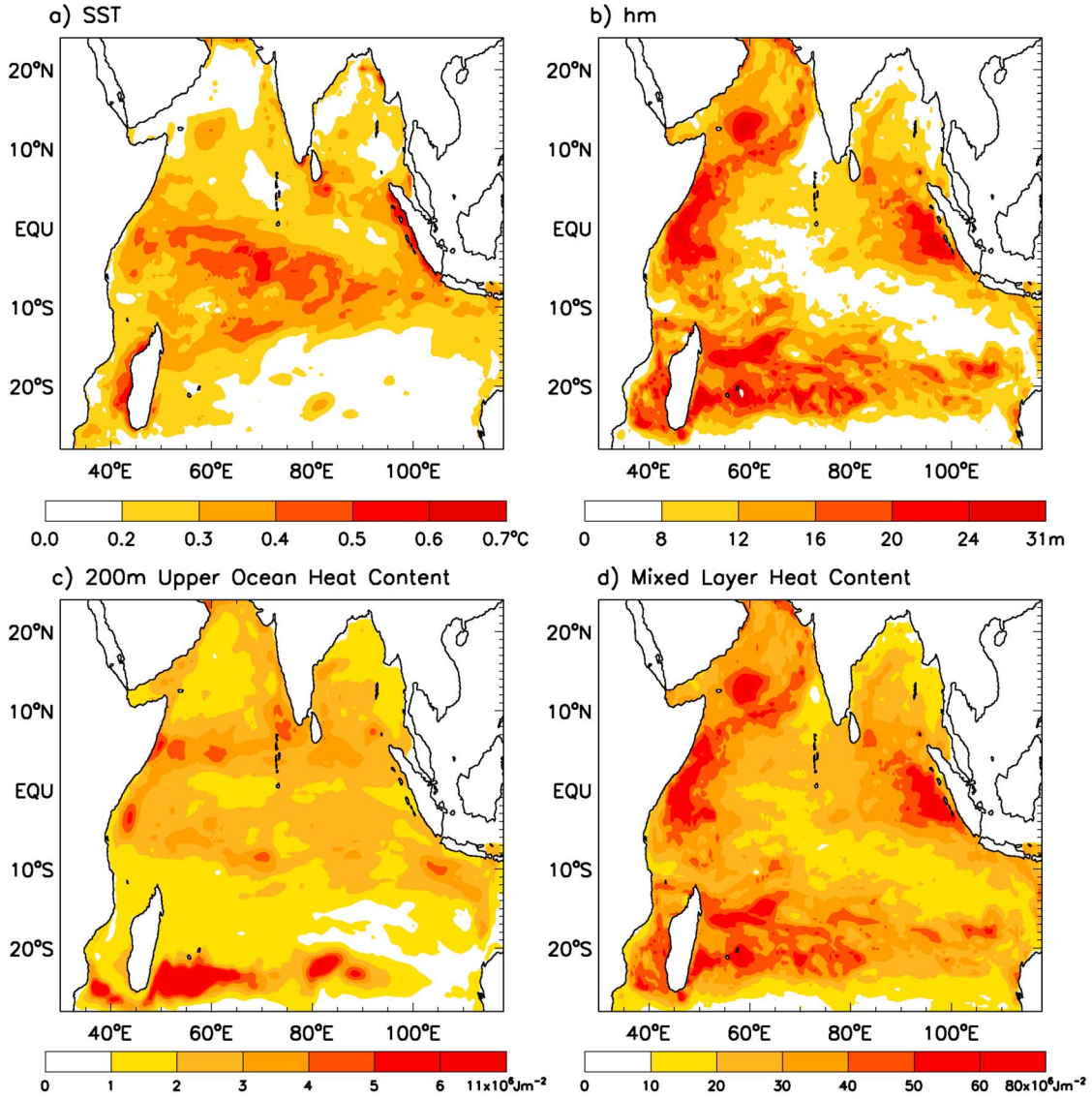

Figure 7. STD of ISO-forced seasonal + interannual HYCOM (a) SST, (b) hm, (c) upper ocean heat content, and (d) mixed layer heat content, calculated from monthly averaged difference solution (MR-EXP1). Units are °C for SST, m for hm, and 10^6 Jm^{-2} for heat content.

(12–31 m; 2.0–8.0 × 10^7 Jm^{-2}), in the eastern equatorial basin (12–31 m; 2.0–8.0 × 10^7 Jm^{-2}) and in the subtropical south IO (15°S–25°S; 8–31 m; 1.0–8.0 × 10^7 Jm^{-2}) (Figures 7b and 7d).

[27] As with the rectification onto the mean, rectification of ISOs onto the variability of hm dominates the mixed layer heat content (Figures 7b and 7d). Consequently, the remainder of this work will focus on the rectification of ISOs onto SST, hm, and upper ocean heat content. As shown above and shall be discussed below, atmospheric ISOs rectify onto the mean, seasonal cycle, and interannual variability of SST, hm, and upper ocean heat content in a number of climatically relevant regions in the IO. In order to further understand the impact of ISO rectification on the IO, the seasonal cycle and the interannual variability of the ISO-forced upper ocean response are evaluated separately. Here, the seasonal cycle is defined as the monthly mean climatology for the period of 2002–2008, and the interannual variability is the deviation from the seasonal cycle.

3.4. ISO Rectification on the Seasonal Cycle of the Upper Ocean

[28] The seasonal cycle of HYCOM difference solution MR-EXP1 provides a measure of the presence and magnitude of atmospheric ISO rectification on seasonal timescales. As with the monthly averages in Section 3.3, all model output variables are low-pass filtered to 105 days before calculating the monthly mean climatologies. For example, the impact of atmospheric ISOs on the seasonal cycle of SST is calculated by low-pass filtering the SST from difference solution MR-EXP1 to 105 days, and then calculating the monthly mean climatology from 2002 to 2008. The same procedure is followed using the other model solution

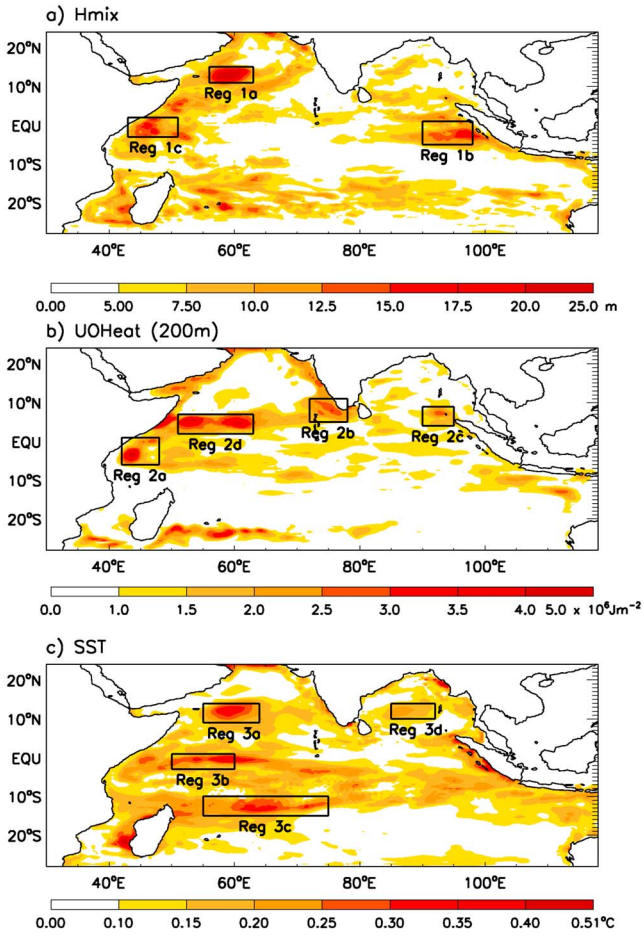

Figure 8. STD of ISO-forced seasonal HYCOM (a) hm, (b) upper ocean heat content, and (c) SST, calculated from difference solution (MR-EXP1). Representative regions with strong ISO-forced seasonal variability are boxed and numbered, and they are discussed in Section 3.4. Units are °C for SST, m for hm, and 10^6 Jm^{-2} for heat content.

differences detailed in Table 2 to determine the rectification of intraseasonal wind, SW radiation, and precipitation onto the seasonal cycle of the upper ocean. The STDs of ISO-forced seasonal variations in SST, hm, and upper ocean heat content all indicate that rectification is present across the IO (Figure 8). The magnitude of rectification onto seasonal variability is relatively large in some areas of the IO. Regions with strong rectification and relatively high model-data correlations are noted by boxes in Figure 8, and they often correspond with the areas of strong seasonal ISO forcing described in Section 1.1. Further analysis of ISO rectification onto seasonal variability focuses on these regions of maximum impact.

[29] As discussed in Section 2.3, it is important to note that the nonlinear response of the ocean to intraseasonal forcing fields can allow the different effects of the forcing fields to interact with each other. We evaluate the impact of these nonlinearities and internal ocean variability on the study results in the sections below.

3.4.1. ISO Rectification on Seasonal hm

[30] Three regions with maximum ISO-forced hm seasonal variability are located in the Arabian Sea (56°E–63°E, 11°N–15°N), the eastern equatorial IO (90°E–98°E, 5°S–1°N), and in the western equatorial IO (43°E–51°E, 3°S–2°N) (Figure 8a). In general, intraseasonal wind has a much larger impact than intraseasonal SW radiation and precipitation on the seasonal cycle of hm in all three regions of interest (Figures 9a–9c, red curves). Intraseasonal wind speed and wind stress contribute to the hm seasonal cycle in amounts that vary by region and timing (Figures 9d–9f, red and blue curves).

[31] The Arabian Sea is a climatologically important region that is strongly impacted by the seasonally changing monsoon winds. In the Arabian Sea, the ISO-forced hm seasonal cycle has minima in April and May (−30.44 m and −28.36 m respectively) and a maximum in October (16.69 m; Figure 9a, black curve). Intraseasonal wind speed, which affects hm by changing the entrainment rate, dominates the springtime minimum and contributes strongly to the fall maximum (Figure 9d, red curve). This is because ISO winds tend to weaken the seasonal monsoon winds during spring when the southwest monsoon begins (Figures 10a–10c), and thus reduce entrainment and shoal the mixed layer. During the monsoon transition period of October, however, mean climatological winds in the Arabian Sea are weak (Figure 10d), and ISO winds strengthen the mean winds (Figures 10e and 10f), causing enhanced entrainment and a thickened mixed layer (Figure 9a). Intraseasonal wind stress, which can rectify onto seasonal hm through anomalous advection and upwelling, also has significant contributions to the deepened hm in October (Figure 9d, blue curve). The effects of SW radiation and precipitation further shallow hm by 5–10 m during spring (Figure 9a, blue and green curves). It is important to note that the sum of the change in hm due to wind, SW radiation, and precipitation does not exactly equal the total rectified hm (Figure 9a, black solid and purple dotted curves), suggesting that the nonlinear response of the ocean to these forcing fields allows different effects to interact. For example, the ISO-associated precipitation can enhance stratification in the region. This enhanced stratification can interact with the weakened winds due to ISOs, thus reducing the entrainment rate and further thinning the hm.

[32] The ISO-induced hm seasonal variations in the east equatorial IO attain minima in February and March (−14.12 m and −13.55 m respectively) and a maximum in September (5.48 m; Figure 9b, black curve). Different from the Arabian Sea, intraseasonal wind stress plays a somewhat larger role in January and February, while intraseasonal wind speed and stress both contribute to the maximum rectified seasonal variations in late summer and fall (Figure 9e).

[33] In the west equatorial IO, ISO rectification onto the hm seasonal cycle has a strong semiannual component that is also seen in the full MR seasonal cycle of hm, which has two maxima and two minima (Figure 9c, solid and dotted black lines). The first maximum occurs in January (12.45 m) during the winter monsoon, and the second occurs in August and September (11.67 m and 11 m, respectively) during the summer monsoon. The first minimum occurs in March (−6.8 m), and the second occurs in November (−12.28 m) during the monsoon transition seasons. Intraseasonal wind stress has a much larger impact on the seasonal hm variations than wind speed during all months with strong ISO rectification in the west equatorial IO (Figure 9f), likely

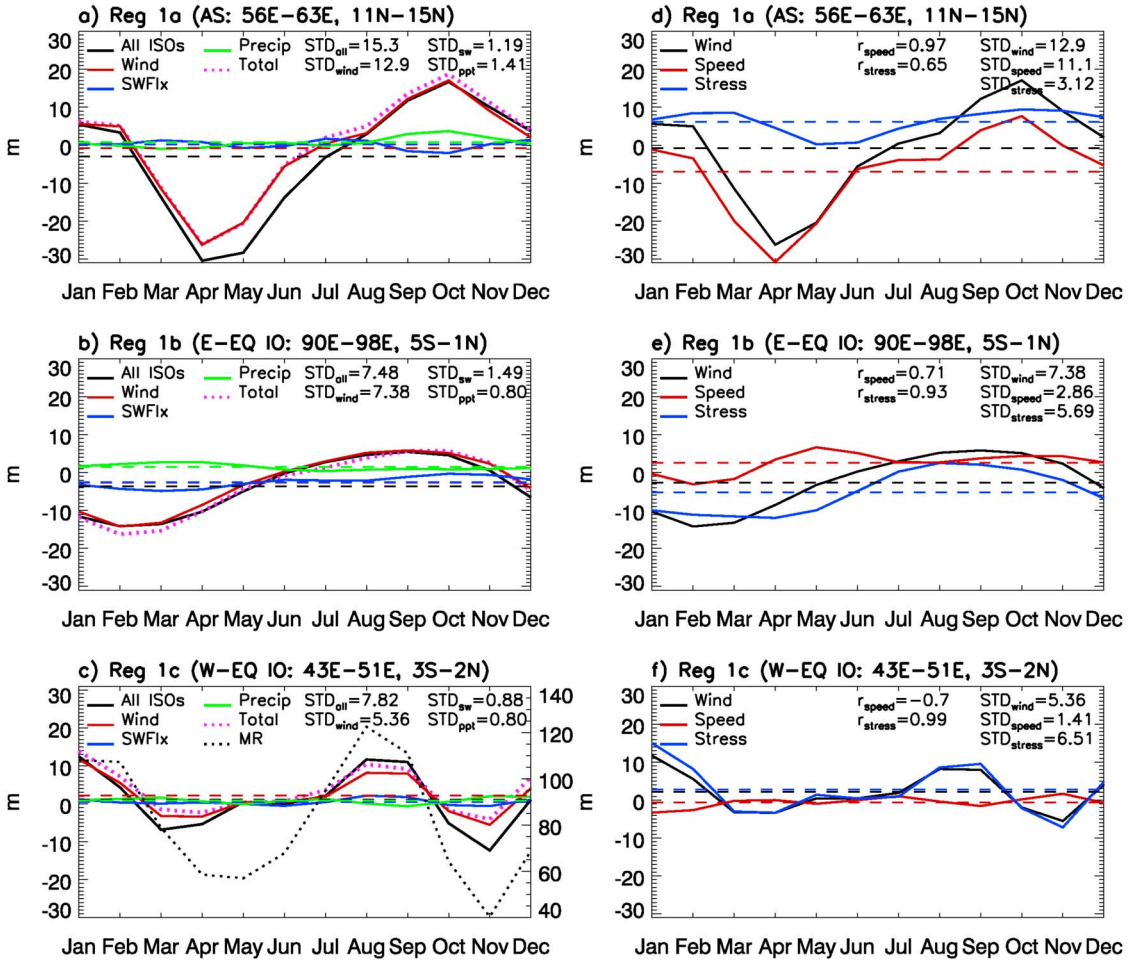

Figure 9. (a) Time series of seasonal hm averaged over the Arabian Sea (Region 1a in Figure 8a), forced by total ISOs (MR-EXP1, black curve), total wind (MR-EXP4, red curve), SW radiation (MR-EXP5, blue curve), and precipitation (MR-EXP6, green curve). The sum of seasonal hm due to each forcing is shown (purple dotted curve). (b) Same as Figure 9a but averaged over the east equatorial IO (Region 1b in Figure 8a). (c) Same as Figure 9a but averaged over the west equatorial IO (Region 1c in Figure 8a). (d) Same as Figure 9a but for seasonal SST forced by total wind (MR-EXP4, black curve), wind speed (EXP3-EXP4, red curve), and wind stress (MR-EXP3, blue curve). (e) Same as Figure 9d but averaged over the east equatorial IO. (f) Same as Figure 9d but averaged over the west equatorial IO. Horizontal lines represent the mean seasonal SSTs from each difference solution. STDs of hm changes due to each intraseasonal forcing are calculated and displayed in the figures, along with the correlation coefficients (r) between total wind hm changes and those due to wind speed and wind stress. Units are m.

because of horizontal advection and changes in mixing associated with shear instabilities (see Section 2.3). As in the Arabian Sea, nonlinearities in the system do allow the effects of the individual forcing fields to interact and affect the full ISO-induced seasonal hm signal in the west equatorial IO (Figure 9c, purple dotted and black solid curves).

3.4.2. ISO Rectification on Seasonal Upper Ocean Heat Content

[34] ISO rectification onto the seasonal cycle of upper ocean heat content occurs in various regions of the IO. Here, we choose four representative regions where the impacts are large: the southwest equatorial IO (42°E–48°E, 6°S–1°N), the southeast Arabian Sea (72°E–78°E, 5°N–11°N), the southern BOB (90°E–95°E, 4°N–9°N), and the southwest Arabian Sea (51°E–63°E, 2°N–7°N) (Figure 8b). In all four regions, ISOs pump heat into the upper ocean on the annual mean, producing positive mean heat content in the upper 200 m (Figures 11a–11c, horizontal black dashed lines; see also Figure 6c). There are, however, significant regionally dependent seasonal variations. As with the impact of hurricanes on the basin [e.g., *Emanuel*, 2001; *Sriver and Huber*, 2007] and the impact of ISOs on the mean state (Section 3.2), atmospheric ISOs appear to act as a heat pump for the tropical north IO. This heat pump effect is dominated by winds associated with ISOs (Figure 11, black and red solid curves). Intraseasonal wind has a much larger impact on the seasonal cycle of upper ocean heat content than intraseasonal SW radiation and precipitation in all regions, especially in the BOB (Figure 11c). Intraseasonal SW radiation does contribute to the seasonal maximum in the southeast Arabian Sea during September (Figure 11b, blue curve). In some regions during some

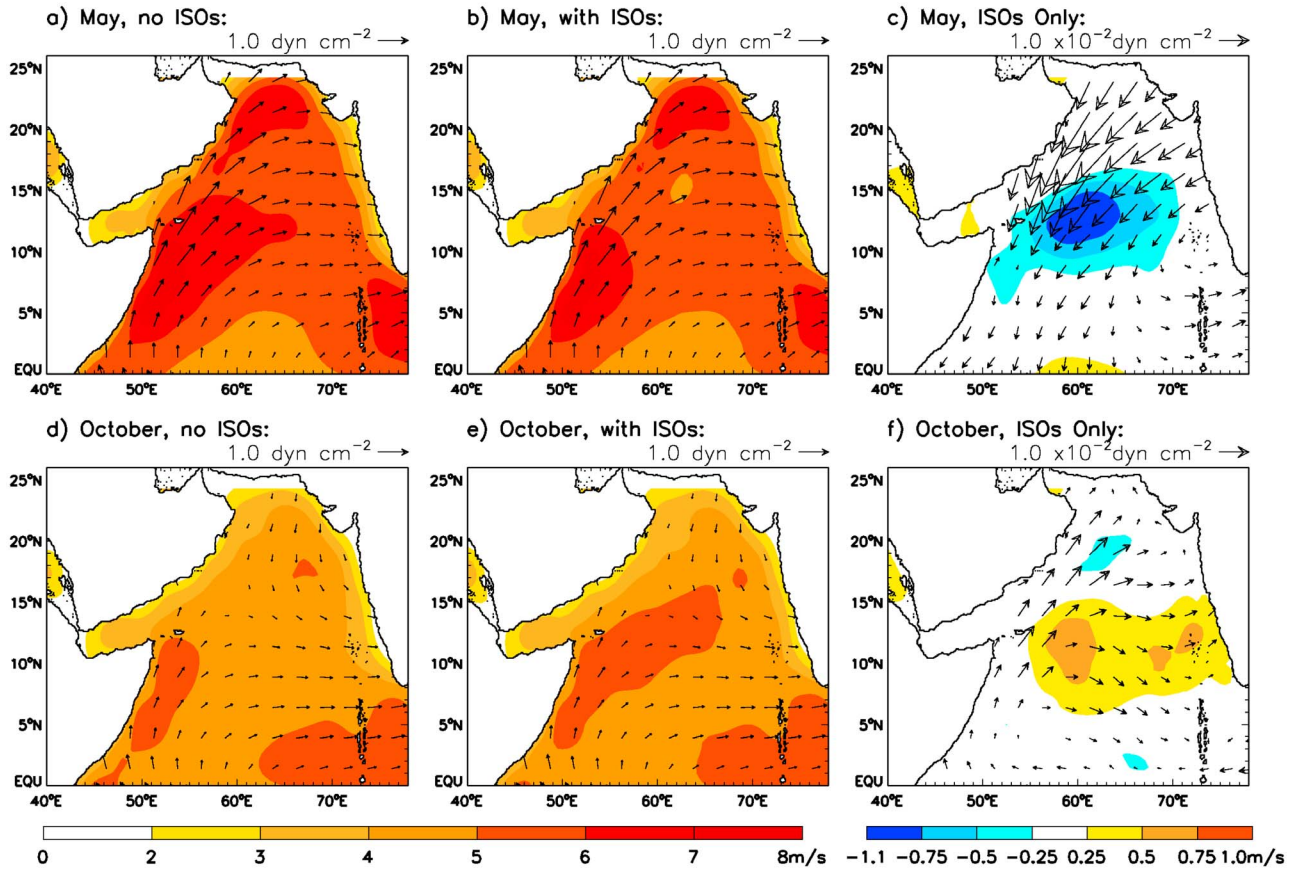

Figure 10. (a) QuickSCAT mean wind speed (shading) and stress (arrows) excluding ISOs, calculated for May (2002–2008) from data that has been low-pass filtered to 105 days. Details about the filter are in Section 2.3. (b) Same as Figure 10a except data is unfiltered and includes ISOs. (c) Same as Figure 10a except only ISO winds are shown. ISO winds are calculated as the difference between full (Figure 10b) and low-passed (Figure 10a) winds. (d) Same as Figure 10a except averaged over October. (e) Same as Figure 10b except averaged over October. (f) Same as Figure 10c except averaged over October. Units are ms^{-1} for wind speed and dyn cm^{-2} for wind stress.

seasons, such as in the western equatorial IO during January–March and in the southeastern Arabian Sea during July–October, the effects of SW radiation and precipitation are non-negligible. Intraseasonal wind stress consistently plays a more important role than wind speed on the seasonal cycle of upper ocean heat content in all regions (Figures 11d–11f, red and blue curves; southwest Arabian Sea not shown). This might be because intraseasonal wind stress increases current shear in the upper ocean and thus enhances shear instabilities and increases mixing. A detailed investigation of the processes that cause this heat pump effect is beyond the scope of this study, but it is an essential component of our future research.

3.4.3. ISO Rectification on Seasonal SST

[35] Atmospheric ISOs have a strong impact on the seasonal variability of SST in a range of climatically important regions of the IO (Figure 8c), including the Arabian Sea (55°E–64°E, 9°N–14°N), the western equatorial IO (50°E–60°E, 3°S–1°N), the southwest IO (55°E–75°E, 15°S–10°S), and the BOB (85°E–92°E, 10°N–14°N). To ensure that this modeled rectification of ISOs onto the SST seasonal cycle is robust, we use HYCOM_InternalEXP to assess the potential impact of oceanic internal variability on our results. Recall from Section 2.3 that interannual variability does not exist in the HYCOM_InternalEXP forcing fields, so any interannual variability in the modeled SST is caused by oceanic internal variability. If the interannual variability of SST from HYCOM_InternalEXP is small in a region, then the modeled seasonal cycle is consistent from year-to-year there, and oceanic internal variability does not play a large role. Analysis of the monthly mean climatology (i.e., the seasonality) of interannual SST variability from HYCOM_InternalEXP shows that oceanic internal variability has little effect on the modeled seasonal cycle of SST in regions where ISO impacts are large, except in the southeast corner of the Arabian Sea during May–October, in the far northeast corner of the west equatorial IO during May–November, and in the southern portion of the southwest IO during July–December (not shown). In all of these small portions of the regions of interest (Figure 8c), the STD of the seasonality of interannual SST variability ranges from 0.2 to 0.5°C. Oceanic internal variability does affect the seasonality of interannual SST variability south of 20°S and along the west coasts of the Arabian Sea and the BOB, with STD ranging from 0.2 to

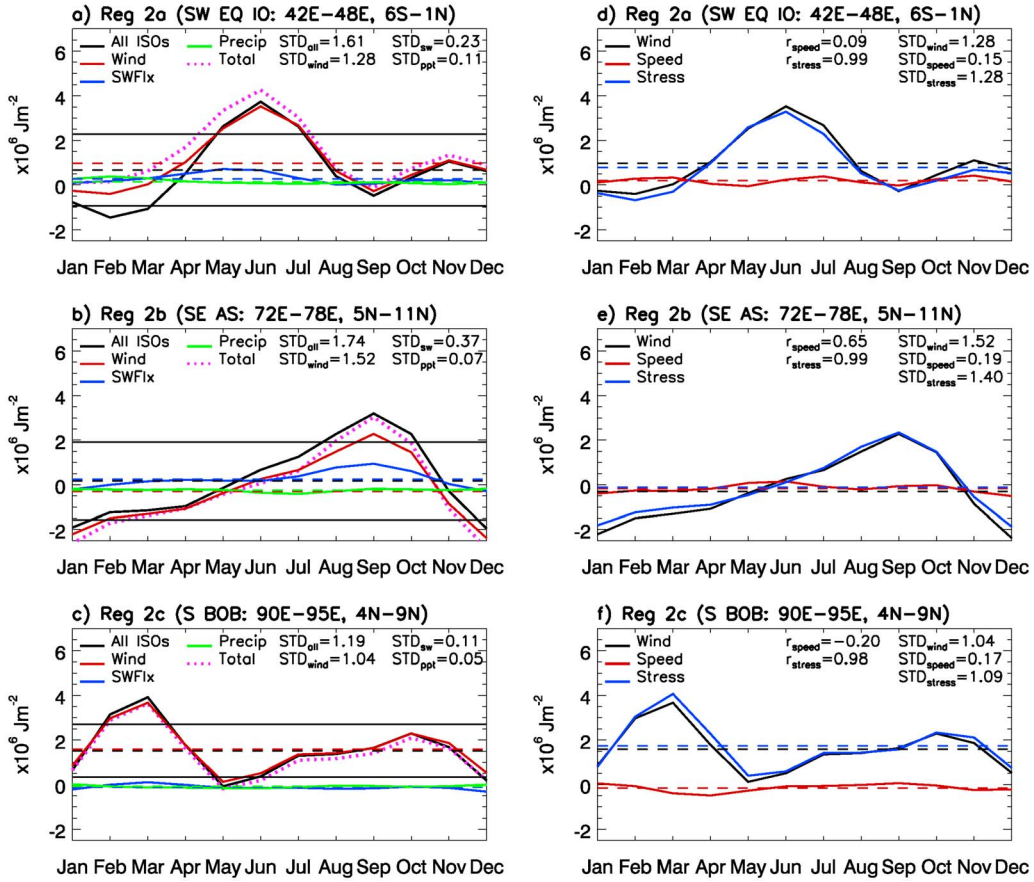

Figure 11. (a) Same as Figure 9a, except for upper ocean heat content averaged over the southwest equatorial IO (Region 2a in Figure 8b). The mean +/− the standard deviation is shown (black thin horizontal lines). (b) Same as Figure 11b except averaged over the southeast Arabian Sea (AS) (Region 2b in Figure 8b). (c) Same as Figure 11a except averaged over the south Bay of Bengal (BOB) (Region 2c in Figure 8b). (d) Same as Figure 9d, except for upper ocean heat content averaged over the southwest equatorial IO. (e) Same as Figure 11d except averaged over the southeast AS. (f) Same as Figure 11d except averaged over the southern BOB. Units are 10^6 Jm^{-2}.

0.5°C (not shown). Taken together, the modeled ISO-forced seasonal cycle of SST is robust in the regions of interest identified in Figure 8c.

[36] Intraseasonal wind consistently has a much larger impact on the total SST seasonal cycle than either intraseasonal SW radiation or precipitation in all four regions (Figures 12a–12c, solid curves; BOB not shown), though the relative importance of intraseasonal wind speed and wind stress varies between the regions (Figures 12d–12f, blue and red solid curves). The consistent dominance of intraseasonal wind speed and stress in causing ISO rectification onto the seasonal cycle of SST suggests that further study is needed to determine how this rectification occurs.

[37] Recall from Section 2.3 that in HYCOM, wind can affect the SST via processes associated with wind stress forcing (upwelling, horizontal advection, and mixing due to shear instabilities) and processes associated with wind speed forcing (THF and entrainment). In HYCOM, all of these processes are represented by nonlinear terms. Because rectification occurs via nonlinear terms in the model equations, all of these 'wind processes' can contribute to the cross-timescale SST rectification observed in Figures 8 and 12. As discussed in Section 1, ISOs are more active in the equatorial region from 15°S–15°N during boreal winter, and farther north in the eastern equatorial IO, the BOB, and the eastern Arabian Sea during boreal summer. The strongest rectification of ISOs onto the seasonal cycle of SST often occurs in these regions with the strongest ISO forcing (Figure 8c). The oscillating wind and convection that are associated with the ISOs alter the total wind speed and stress, convection, and precipitation. Impacts of these changes on SST can cross timescales because of the nonlinear processes described in Section 2.3. Each of the wind processes is estimated as directly as possible to further evaluate its relative importance in the rectification of atmospheric ISOs onto longer-timescale SST variability. The complexity of HYCOM's model equations makes it difficult to exactly isolate the impact of an individual process on SST, hm and upper ocean heat content. Despite these limitations, the diagnostics described below provide a more in-depth understanding of the processes by which intraseasonal wind can impact seasonal-to-interannual SST variability.

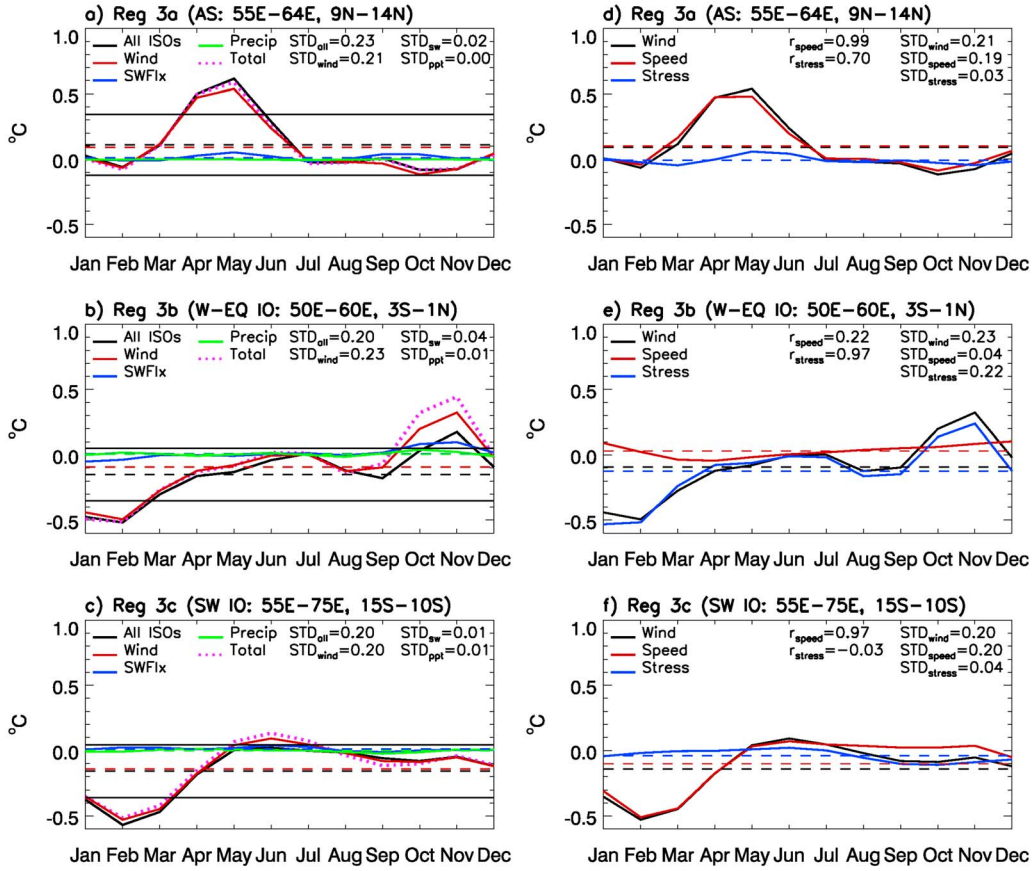

Figure 12. (a) Same as Figure 9a except for SST averaged over the AS (Region 3a in Figure 8c). (b) Same as Figure 12a except averaged over the west equatorial IO (Region 3b in Figure 8c). (c) Same as Figure 12a except averaged over the southwest IO (Region 3c in Figure 8c). (d) Same as Figure 9d, except for SST averaged over the AS. (e) Same as Figure 12d except averaged over the west equatorial IO. (f) Same as Figure 12d except averaged over the southwest IO. Units are °C.

[38] Entrainment and THF are the two processes by which intraseasonal wind speed can affect the seasonal SST cycle, and we evaluate the relative strength of each. Recall from Section 2.3 that in this work, entrainment cooling is primarily determined by the local time derivative of a depth h, which in turn is dependent on the turbulent frictional velocity (u*) calculated using only wind speed. Hm due only to wind speed is therefore used to diagnose the presence of entrainment in the model output – increased (decreased) entrainment cooling causes a thickening (thinning) of the mixed layer as increasing (decreasing) amounts of cool subsurface water are entrained into the surface mixed layer. The impact of the seasonal rectification of intraseasonal wind speed on entrainment is estimated by calculating the seasonal cycle of hm due only to intraseasonal wind speed (model difference solution EXP3-EXP2; Table 2).

[39] The impacts of intraseasonal wind speed on THF are calculated with the formula

$$THF = HF_{EXP2} - HF_{EXP3}, \tag{3}$$

where *HF* is the net heat flux from EXP2 (low-pass wind stress) and EXP3 (low-pass wind stress and speed). In HYCOM, the model output net heat flux is the sum of THF and net radiative flux, where net radiative flux is an ISCCP-FD model forcing field. The net radiative flux portion of HF is the same for EXP2 and EXP3; only the turbulent heat fluxes can vary between the two experiments. Taking the difference between the two HF quantities isolates the changes in THF due only to intraseasonal wind speed. Increasingly negative THF indicates that more energy is leaving the ocean due primarily to increased evaporation. Because THF takes time to warm or cool the ocean, a one month lag is applied in the following analysis. For example, the THF in April is used to evaluate the contribution of THF to an SST anomaly in May. Various lags are tested, and the one month lag provides the most reasonable result.

[40] Changes in SST due to intraseasonal wind stress-induced upwelling are estimated using the formula

$$dTup_{3d} = w_{EISO}\frac{d}{dz}(T - \bar{T})dt, \tag{4}$$

where $dTup_{3d}$ is the change in SST over 3 days due to upwelling; $w_{E\ ISO}$ is the Ekman pumping velocity due to intraseasonal wind stress; $\frac{d}{dz}(T - \bar{T})$ is the change in temperature over the depth of the mixed layer; and dt is the time

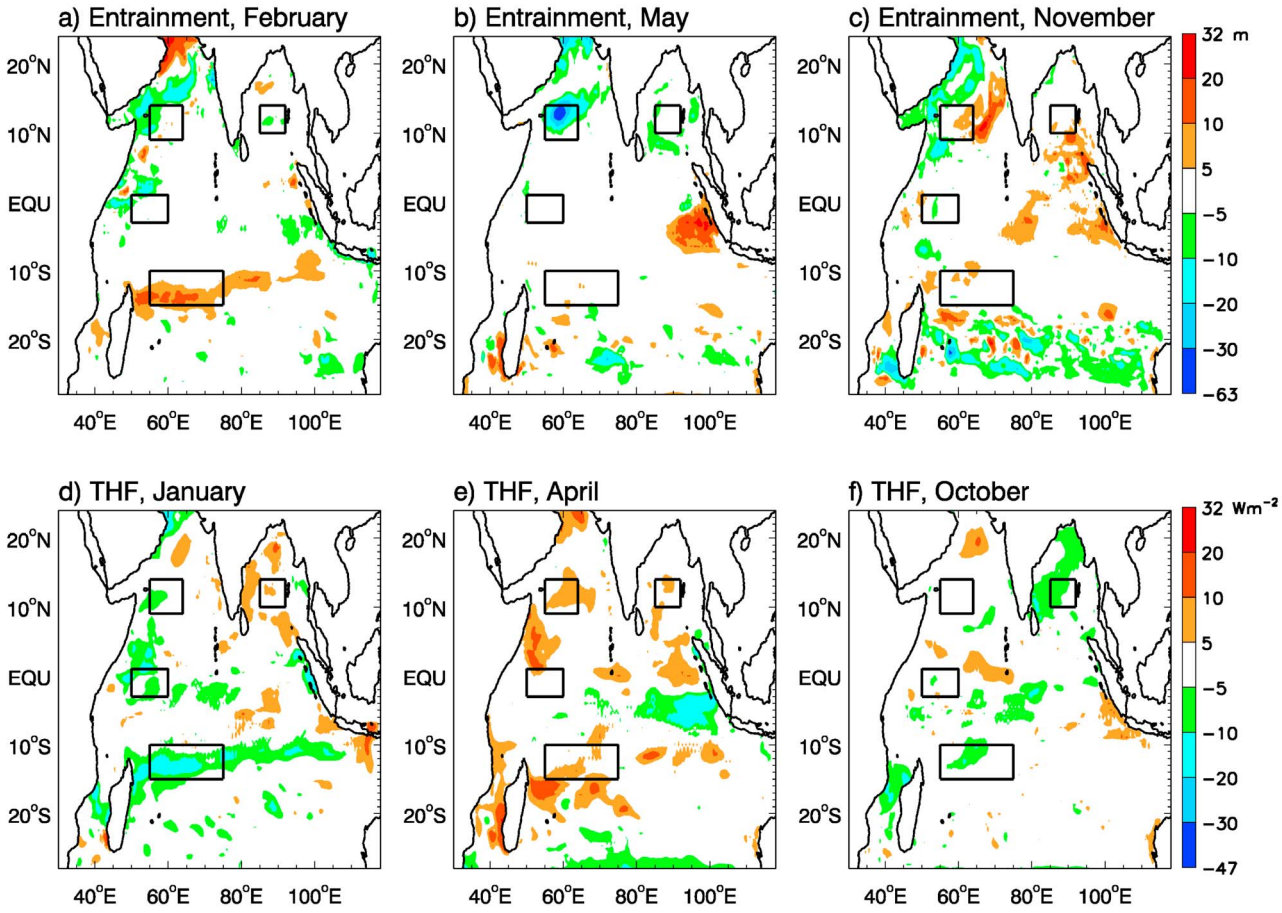

Figure 13. (a–c) Selected months of the seasonal cycle of hm due only to intraseasonal wind speed (HYCOM difference solution EXP3-EXP4). Changes in hm indicate the presence of entrainment. Boxed regions correspond to the SST representative regions of interest in Figure 8c. See Section 3.4.3 for more details about this calculation. Units are m. (d–f) Same as Figures 13a–13c but for turbulent heat flux (THF). Units are Wm^{-2}.

step (3 days). The Ekman pumping velocity associated with intraseasonal wind stress curl is calculated with the equation

$$w_{EISO} = \frac{d}{dx}\left(\frac{\tau_{yISO}}{f}\right) - \frac{d}{dy}\left(\frac{\tau_{xISO}}{f}\right), \quad (5)$$

where x is longitude, y is latitude, f is the Coriolis parameter at a given latitude, and τ_{xISO} and τ_{yISO} are intraseasonal zonal and meridional wind stress, respectively.

[41] Intraseasonal wind stress can also change SST via horizontal advection. This is assessed with the equation

$$dTadv_{3d} = -\left[u_{ISO}\frac{d}{dx}(T-\bar{T}) + v_{ISO}(T-\bar{T})\right]dt, \quad (6)$$

where u_{ISO} and v_{ISO} are intraseasonal wind stress-forced currents, x and y are longitude and latitude, dt is the time step (3 days), and $dTadv_{3d}$ is the change in SST over 3 days due to horizontal advection.

[42] In the Arabian Sea and the BOB, the ISO-forced seasonal SST variations have a maximum in April and May (Figure 12a, black curve; BOB not shown), indicating that rectification is generally large each April and May from 2002 to 2008. The similar timing in the Arabian Sea and the BOB is likely due to the strong influence of summer ISOs in the two regions. Because SSTs in the Arabian Sea already exceed 28°C, the ISO-forced seasonal cycle peak of 0.6°C in May can have an important effect on convection there. Consistent with the rectified hm, the large amplitude of the rectified SST seasonal cycle during April and May in the Arabian Sea and the BOB is mostly caused by intraseasonal wind speed (Figure 12d, red curve), which suggests that anomalous THF and entrainment cooling are the major causes of the modeled seasonal warming, shortly before the onset of the Indian summer monsoon.

[43] The seasonal variations of intraseasonal wind speed-forced hm indicate that reduced entrainment causes the mixed layer in the Arabian Sea (BOB) to shoal by up to 63 m (<5 m) in May (Figure 13b). At the same time, the ISO-forced THF in the Arabian Sea and the BOB is 0–10 W/m^2 in April (Figure 13e). The seasonal cycles of upwelling and horizontal advection (Tup and Tadv) are negligible in the Arabian Sea and in the BOB in April and May (Figures 14b and 14e), which is expected because intraseasonal wind stress does not play a large role in these seasonal cycle peaks. Note that the magnitude of the seasonal SST peak is greater in the Arabian

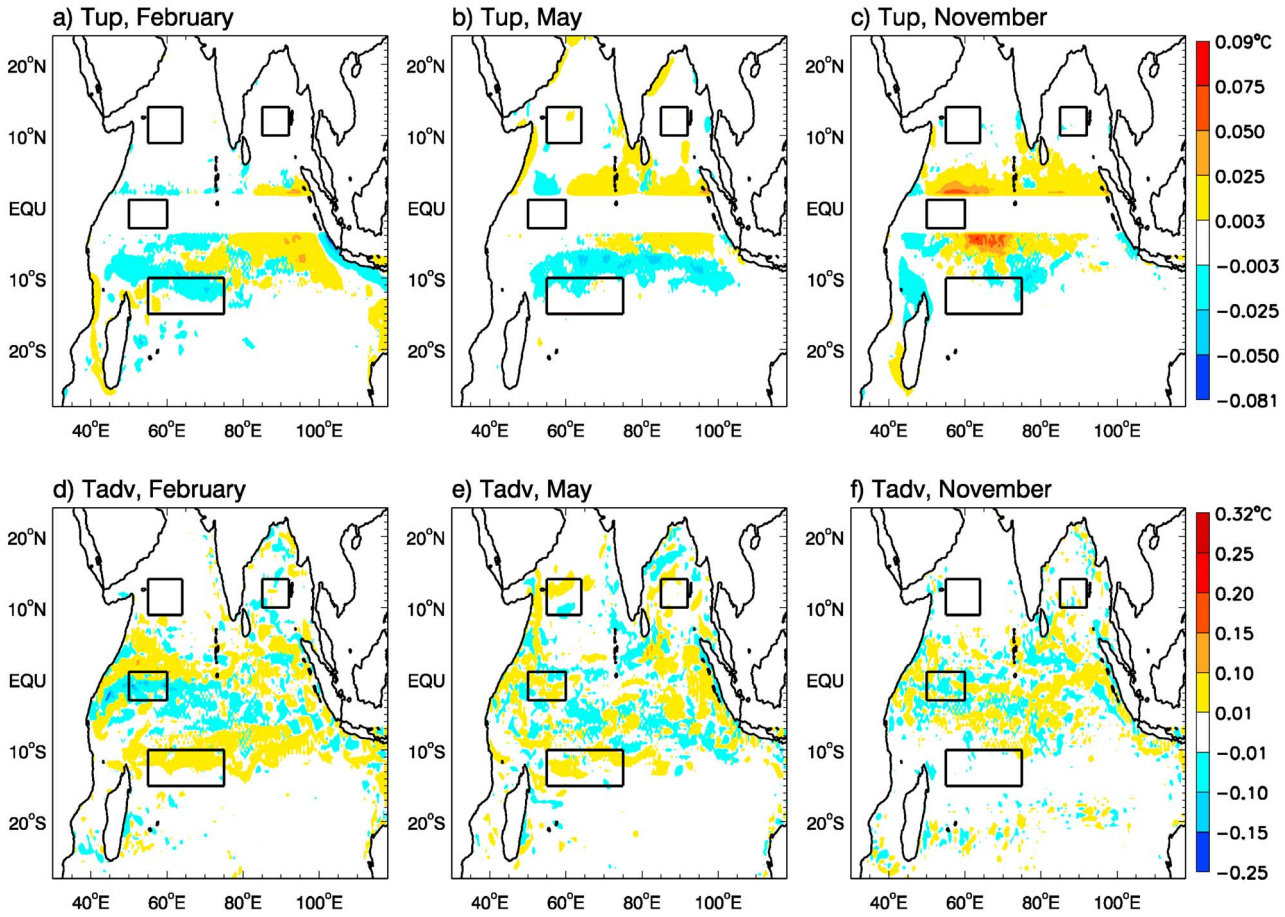

Figure 14. (a–c) Selected months of the seasonal cycle of the change in SST (dT) due only to upwelling forced by intraseasonal wind stress. Boxed regions correspond to the SST representative regions of interest in Figure 8c. See Section 3.4.3 for more details about this calculation. (d–f) Same as 14a–14c but due only to horizontal advection forced by intraseasonal wind stress. Units are °C.

Sea than in the BOB, which explains the larger magnitudes of hm and THF in the Arabian Sea. Put together, the seasonal cycle of SST in the Arabian Sea and the BOB peaks during the April and May inter-monsoon period. ISOs weaken the seasonal winds, causing reduced entrainment (shoaling hm) and reduced evaporation (positive THF), and resulting in consistently warmer SSTs (Figures 9, 10, 12, 13, and 14).

[44] In the west equatorial IO, the ISO-forced SST seasonal cycle has a minimum in January (−0.47°C) and February (−0.51°C), and a maximum in November (0.17°C) (Figure 12b, black curves). Different from the Arabian Sea, intraseasonal wind stress consistently causes the majority of the rectified seasonal cycle, though intraseasonal wind speed does contribute to the November SST peak (Figure 12e, red and blue curves). Nonlinearities of the oceanic system do have some impact on the seasonal cycle of SST induced by ISOs in the west equatorial IO during November (Figure 12b, purple dotted and black solid curves). The ISO wind speed-forced THF and entrainment play a negligible role in the cooling during January and February (Figures 13a and 13d), while entrainment is somewhat reduced during the November warming (Figure 13c). The ISO wind stress-induced hm thickens by ∼9 m in January and thins by ∼4 m in November (not shown), indicating that entrainment due to shear instability associated with ISO wind stress forcing contributes to the cooling as well. The rectified seasonal dT due to horizontal advection ranges from −0.1°C to −0.25°C during January and February, and it is mixed during November (Figures 14d and 14f). Horizontal advection and shear instability due to intraseasonal wind stress both contribute to the rectified seasonal SST minimum (maximum) in January and February (November), with entrainment due to intraseasonal wind speed contributing slightly during November.

[45] In the southwest IO, the ISO-forced SST seasonal variability has a minimum from January–March, with peak cooling of 0.56°C in February (Figure 12c, black curve). As in the Arabian Sea, ISO-forced wind speed has a much larger impact than wind stress during each month (Figure 12f, red and blue curves). Consistent with the dominance of intraseasonal wind speed, intraseasonal wind stress-induced upwelling and horizontal advection are weak (Figures 14a and 14d). The increased intraseasonal wind speed in January and February causes increased entrainment cooling (thickened hm) and negative THF (Figures 13a and 13d), which cause rectified seasonal SST cooling. Given that the wintertime MJOs have large amplitudes in this region, these

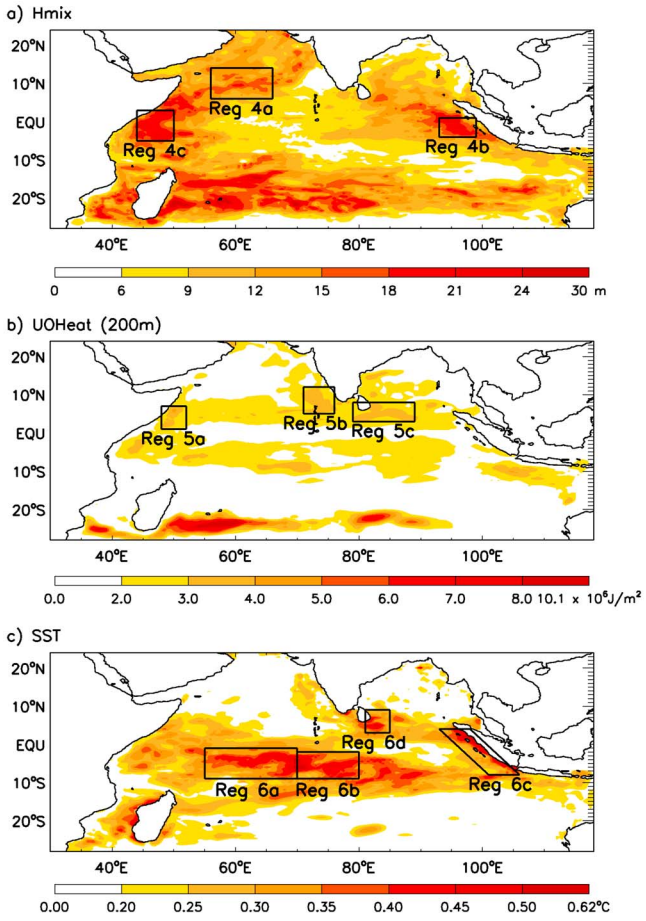

Figure 15. Same as Figure 8 but for interannual (a) hm, (b) upper ocean heat content, and (c) SST. Units are °C for SST, m for hm, and 10^6 Jm^{-2} for heat content.

rectified processes are physically reasonable and thus likely to be real, even though the impacts of ISOs worsen the model/data comparison (Section 3.1 and Figure 5b). ISOs worsen the simulated SST because of the mean bias of HYCOM in this region, where the HYCOM hm is thinner and the SST is cooler than observed (Figures 3 and 4). Consequently, further cooling by ISOs will increase the model/data discrepancy.

3.5. ISO Rectification on Interannual Upper Ocean Variability

[46] It is clear from Figure 7 that atmospheric ISOs rectify onto both the seasonal and the interannual variability of SST, hm, and upper ocean heat content. In order to better understand the rectification of ISOs onto the interannual variability of the upper IO, the interannual variability is calculated with the equation

$$T_{iann} = T_{monavg} - T_{monclim}, \quad (7)$$

where T_{monavg} and $T_{monclim}$ are the monthly average and monthly climatology time series, respectively, of 3-day model output data that has been low-pass filtered to 105 days. Monthly averaging the data (i.e., average of Jan 2002, average of Feb 2002, … average of December 2008) isolates the seasonal and interannual ocean response. Because the monthly mean climatology (i.e., average January 2002–2008) isolates the seasonal cycle of the ocean response, removing it from the low-pass 105 day filtered, monthly averaged data isolates the interannual ocean response. If data from difference solution MR-EXP1 is used in the equation above, then the atmospheric ISO-forced interannual variability of the ocean is isolated.

[47] As with the seasonal cycle analysis in Section 3.4, the standard deviations of ISO-forced interannual hm, upper ocean heat content, and SST are used to identify regions with the strongest rectified interannual variability, which are noted with boxes in Figure 15. Time series of region-averaged ISO-forced interannual SST, hm, and upper ocean heat content are used to determine the timing of strong rectification (Figures 16–18). Months with strong rectification are those in which the signal change is greater than one standard deviation, and they are evaluated to better understand the processes controlling the rectification of atmospheric ISOs onto interannual upper ocean variability.

3.5.1. ISO Rectification on Interannual hm

[48] Atmospheric ISOs exhibit strong rectification onto interannual hm in many regions of the IO. Here, we choose three regions of interest: the Arabian Sea (56°E–66°E, 6°N–14°N), the east equatorial IO (93°E–99°E, 4°S–1°N), and the west equatorial IO (44°E–50°E, 5°S–3°N) (Figure 15a). These regions are similar to those with strong seasonal hm rectification (Figure 8a). The consistent rectification across timescales in these regions suggests that the interannual hm variability exists as changes in the amplitude of consistent hm shoaling or deepening from year to year. As with the rectification of atmospheric ISOs onto the seasonal cycle, the rectified interannual hm is dominated by intraseasonal wind, rather than by intraseasonal SW radiation or precipitation (Figures 16a–16c, solid curves). However, there are exceptions in some regions and during some months. For example, during January 2006 in the west equatorial IO, intraseasonal precipitation contributes to the interannual hm signal (Figure 16c). The relative importance of ISO-forced wind speed and wind stress varies from region to region and from month to month, but it is generally consistent with the results from the seasonal rectification analysis (Section 3.4.1 and Figures 9d–9f and Figures 16d–16f). ISO rectification onto interannual hm also exhibits strong seasonality: strong rectification tends to occur during boreal fall and winter months in the Arabian Sea and the east equatorial IO, while it occurs during boreal spring and summer in the west equatorial IO (Figures 16a–16c, black curves).

[49] In the Arabian Sea, strong ISO-forced hm rectification occurs in October 2004 when hm deepens by 17.77 m, and in November 2007 when hm shoals by 12.37 m (Figure 16a, black curve). Nonlinearities in the process interactions do have some impact on the October 2004 signal (Figure 16a, purple dotted and black solid curves). As with the rectified seasonal cycle in the Arabian Sea (Section 3.4.1), changes in the entrainment rate due to intraseasonal wind speed play a much larger role in the rectified interannual hm signal during both months than upwelling, horizontal advection, and shear-induced mixing due to wind stress (Figure 16d, red and blue curves). Both intraseasonal wind stress and wind speed contribute approximately equally to the deepened hm in October 2004.

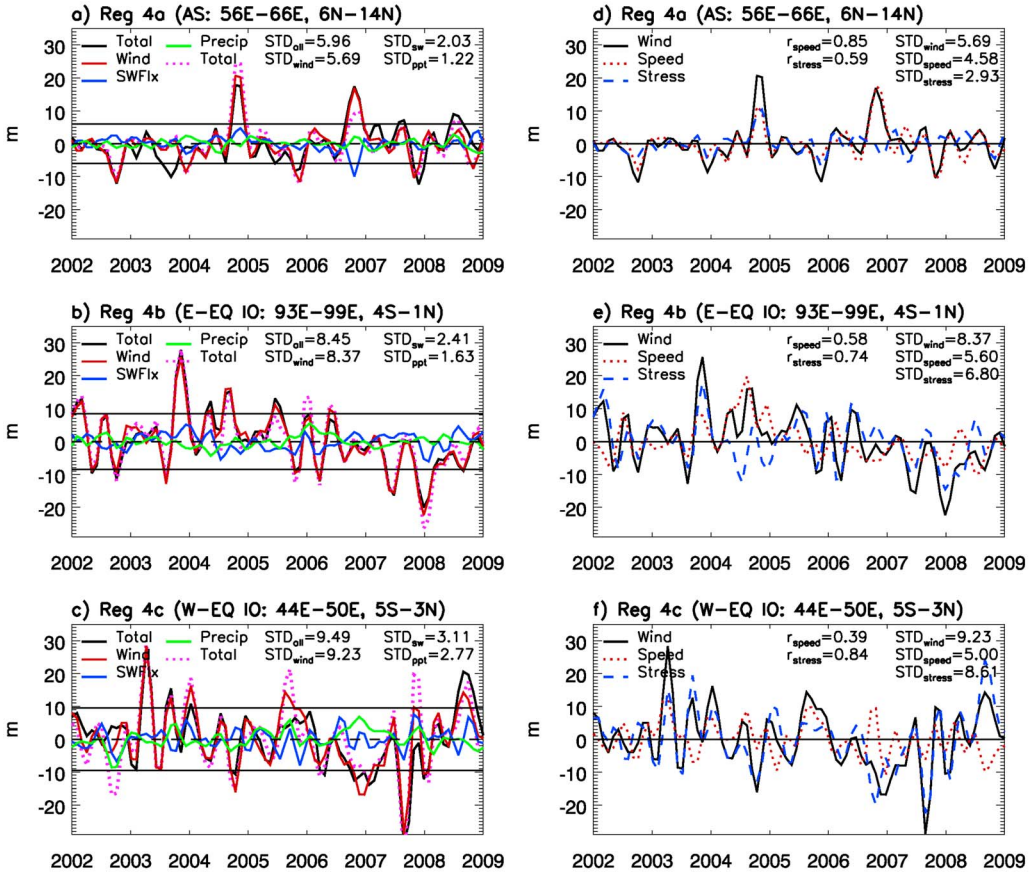

Figure 16. Same as Figure 9 except for interannual hm from 2002 to 2008 averaged over (a and d) the AS (Region 4a in Figure 15a), (b and e) the east equatorial IO (Region 4b in Figure 15a), and (c and f) the west equatorial IO (Region 4c in Figure 15a). Horizontal lines in Figures 16a–16c represent 1 STD for ISO-forced interannual hm, while those in Figures 16d–16f represent zero. Details about calculating interannual variability are in Section 3.5. Units are m.

[50] Strong ISO-forced interannual hm variability occurs in the east equatorial IO during November 2003 (hm thickens by 27.86 m) and December 2007 (hm shoals by 20 m) (Figure 16b, black curve). As in the Arabian Sea, nonlinearities do have some impact on the rectified signal in December 2007 (Figure 16b, purple dotted and black solid curves). Consistent with the rectified hm seasonal cycle in the east equatorial IO, intraseasonal wind stress has a slightly larger impact during both months than changing entrainment due to intraseasonal wind speed (Figure 16e, red and blue curves).

[51] The strongest ISO-forced interannual hm signal in the west equatorial IO occurs during April 2003 (hm thickens 28.23 m) and August 2007 (hm shoals 32 m) (Figure 16c, black curve). The effect of ISO precipitation is weak during the August 2007 shoaling, but it plays a more significant role during early and mid 2006 (Figure 16c, green curve). Different from the processes controlling seasonal hm rectification, ISO-forced wind stress and speed both contribute equally to the April 2003 thickening. However, intraseasonal wind stress plays a much larger role than wind speed during August 2007, which is consistent with the dominant processes that controlled seasonal hm rectification in the region (Figures 9c, 9f, 16c, and 16f).

3.5.2. ISO Rectification on Interannual Upper Ocean Heat Content

[52] Strong ISO-forced interannual upper ocean heat content variability occurs in the IO within 15°S–15°N. Here, we choose three regions with maximum interannual variability: the west equatorial IO (48°E–52°E, 1°N–7°N), the southeast Arabian Sea (71°E–76°E, 5°N–12°N), and near Sri Lanka in the southwest BOB (79°E–89°E, 3°N–8°N) (Figure 15b). ISO rectification onto seasonal upper ocean heat content is also large in the southeast Arabian Sea (Figure 8b), indicating that the interannual variability there represents changes in the amplitude of the rectified seasonal signal from year to year. In general, strong interannual upper ocean heat content rectification occurs during boreal fall and winter when wintertime MJOs are strong, and this rectification is dominated by wind stress in all three regions (Figure 17). The deterministic role played by wind stress is consistent with the rectified seasonal variability of upper ocean heat content discussed in Section 3.4.2. However, intraseasonal SW radiation and precipitation do contribute significantly during some months, as in the western equatorial IO during boreal fall in 2003 and 2006 (Figures 17a–17c, blue and green curves).

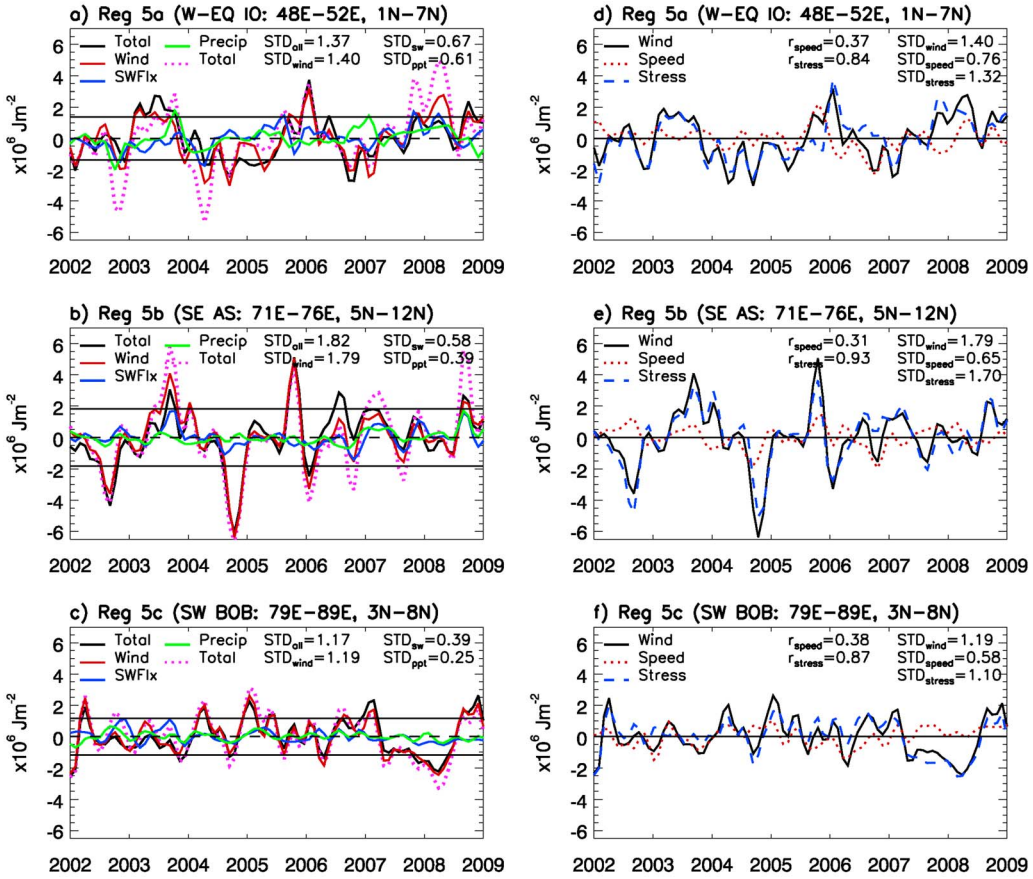

Figure 17. Same as Figure 16 except for interannual upper ocean heat content averaged over (a and d) the west equatorial IO (Region 5a in Figure 15b), (b and e) the southeast AS (Region 5b in Figure 15b), and (c and f) the southwest BOB (Region 5c in Figure 15b). Units are 10^6 Jm^{-2}.

3.5.3. ISO Rectification on Interannual SST

[53] The largest ISO impacts on interannual SST are confined to 10°S–10°N. Representative regions where ISO-forced interannual SST anomalies obtain their maxima include the west equatorial IO (55°E–70°E, 9°S–1°S), the central IO (70°E–80°E, 9°S–2°S), the east equatorial IO (94°E–99°E, 3°S–3°N), and the Sri Lanka Dome region (81°E–85°E, 3°N–9°N) (Figure 15c). As in Section 3.4.3, we use HYCOM_InternalEXP to evaluate the impacts of internal ocean variability on the modeled rectified signal. Analysis of HYCOM_InternalEXP shows that oceanic internal variability has little effect on the modeled interannual variability of SST in the regions listed above, although it does play a role in the southern IO (70°E–115°E, 25°S–20°S) and along the far western Arabian Sea and BOB (not shown). That is, the modeled rectification of ISOs onto interannual SST variability is robust in the regions of interest shown in Figure 15c. Nonlinearities in the interactions of ISO processes do occasionally contribute to the modeled signal (Figures 18a–18c, purple dotted and black solid curves).

[54] The strongest rectification tends to occur in all of the regions of interest during the boreal late winter, spring, and summer months, with the exception of rectified cooling in the Sri Lanka Dome region during October 2004 (Figures 18a–18c, black curves; Sri Lanka Dome not shown). Generally, entrainment and THF due to intraseasonal wind speed, and upwelling, horizontal advection and shear-induced mixing due to intraseasonal wind stress, have much larger impacts on the rectified interannual SST signal than either intraseasonal SW radiation or precipitation (Figures 18a–18c, solid curves). Intraseasonal SW radiation and precipitation do sometimes affect the interannual SST variability. For example, intraseasonal SW radiation contributes to the modeled interannual warming in the central IO during February 2008 (Figure 18b, black curve). The relative importance of intraseasonal wind speed and stress varies between regions and months (Figures 18d–18f, red dotted and blue dashed curves). As with the rectified seasonal SST analysis (Section 3.4.3), the apparent dominance of wind-forcing lends itself to further study. The impacts of intraseasonal wind processes (entrainment and THF associated with wind speed; and upwelling, horizontal advection, and shear instability induced mixing associated with wind stress) on interannual SST variability are estimated with the same equations used in the regional SST seasonal cycle analysis (Section 3.4.3). Instead of isolating the seasonal impacts with monthly climatologies, the interannual impacts are isolated using equation (7).

[55] During June 2003, strong cooling of ~0.33°C occurs in both the west and east equatorial IO regions (Figures 18a and 18c, black curves), due approximately equally to increased intraseasonal wind speed and wind stress (Figures 18d and 18f, color curves). In the west equatorial

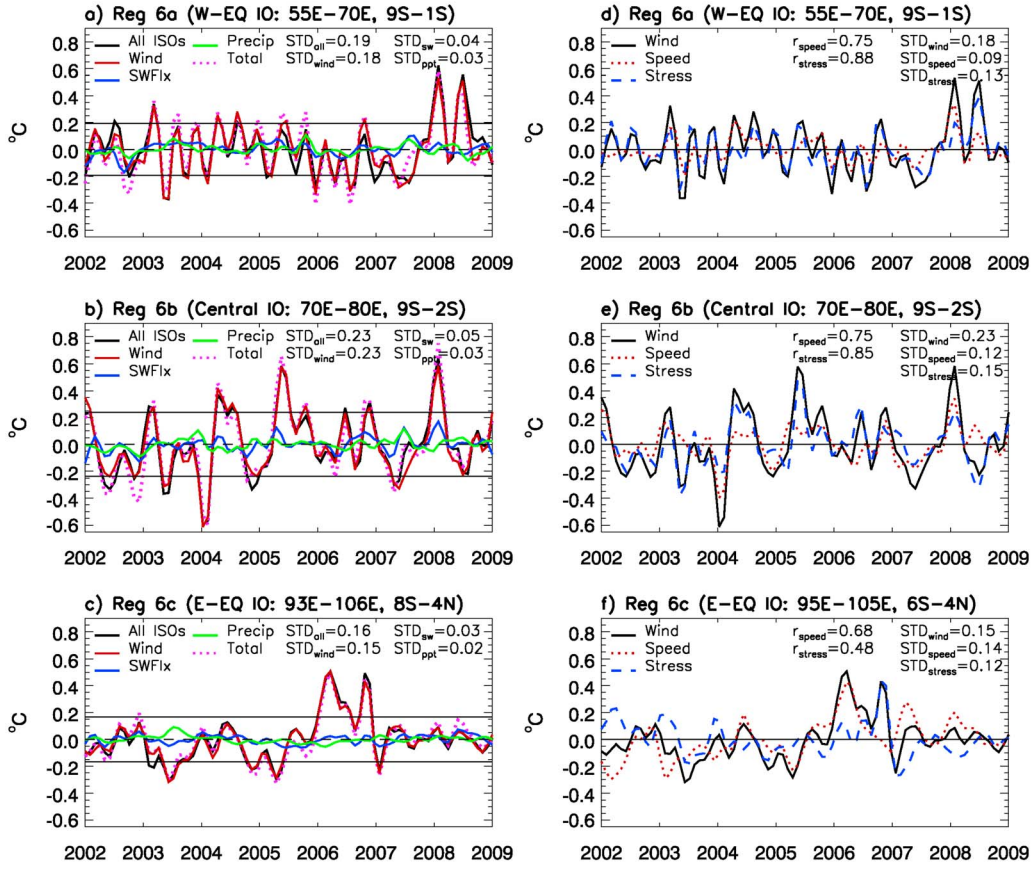

Figure 18. Same as Figure 16 except for SST averaged over (a and d) the west equatorial IO (Region 6a in Figure 15c), (b and e) the central IO (Region 6b in Figure 15c), and (c and f) the east equatorial IO (Region 6c in Figure 15c). Units are °C.

IO, negative THF and upwelling cooling play much larger roles than entrainment cooling and horizontal advection, while entrainment, THF, upwelling, and horizontal advection all contribute in the east equatorial IO (Figures 19a, 19d, 20a, and 20d). During other months in all of the regions of interest, intraseasonal wind speed has a larger impact than wind stress (and vice versa) on the interannual SST rectification. The dominance of processes like entrainment and upwelling vary from month-to-month. For example, strong rectified cooling (0.6°C) occurs during January 2004 in the central equatorial IO (Figure 18b, black curve). The reduced SSTs are most strongly forced by THF due to intraseasonal wind speed, and to a lesser extent by horizontal advection and upwelling due to intraseasonal wind stress (Figures 19b, 19e, 20b, and 20e). In contrast, horizontal advection does not contribute significantly to the rectified warming (~0.63°C) found in the west and central equatorial IO during January 2008 (Figures 18a, 18b, and 20f). These increased SSTs are most strongly forced by entrainment and THF due to intraseasonal wind speed, and by upwelling due to intraseasonal wind stress (Figures 19c, 19f, and 20c).

4. Discussion and Conclusions

[56] In the present study, the impacts of atmospheric ISOs on the seasonal cycle and interannual variability of the upper layers of the IO are examined by performing a hierarchy of experiments using HYCOM (Table 1). Differences between experiment solutions (Table 2) allow us to isolate the ocean response to full ISOs and to a range of individual intraseasonal forcing fields, which are associated with specific oceanic processes in HYCOM. In general, the model indicates that atmospheric ISOs do rectify onto the mean and seasonal-to-interannual variability of SST, hm, and upper ocean heat content, and the impacts of this rectification vary regionally but generally follow regions with the strongest ISO forcing (Figures 6 and 7). Regions with the maximum ISO impact on the mean state and standard deviation of hm and mixed layer heat content are almost identical (Figures 6b, 6d, 7b, and 7d), indicating that hm is the dominant factor in determining mixed layer heat content.

[57] Atmospheric ISOs have a large impact on the modeled seasonal cycle and interannual variability of SST, hm, and upper ocean heat content in a number of climatically relevant regions of the IO (Figures 8 and 15). Regions with the strongest ISO rectification are identified and boxed in Figures 8 and 15. Analysis of experiment HYCOM_InternalEXP, which is forced only with monthly climatology, demonstrates that the modeled rectification is robust and not greatly influenced by model internal variability in these regions of interest. Further study focuses on the strength of rectification in these regions, and on the processes that cause it.

[58] In general, entrainment and THF due to intraseasonal wind speed, and upwelling, horizontal advection, and

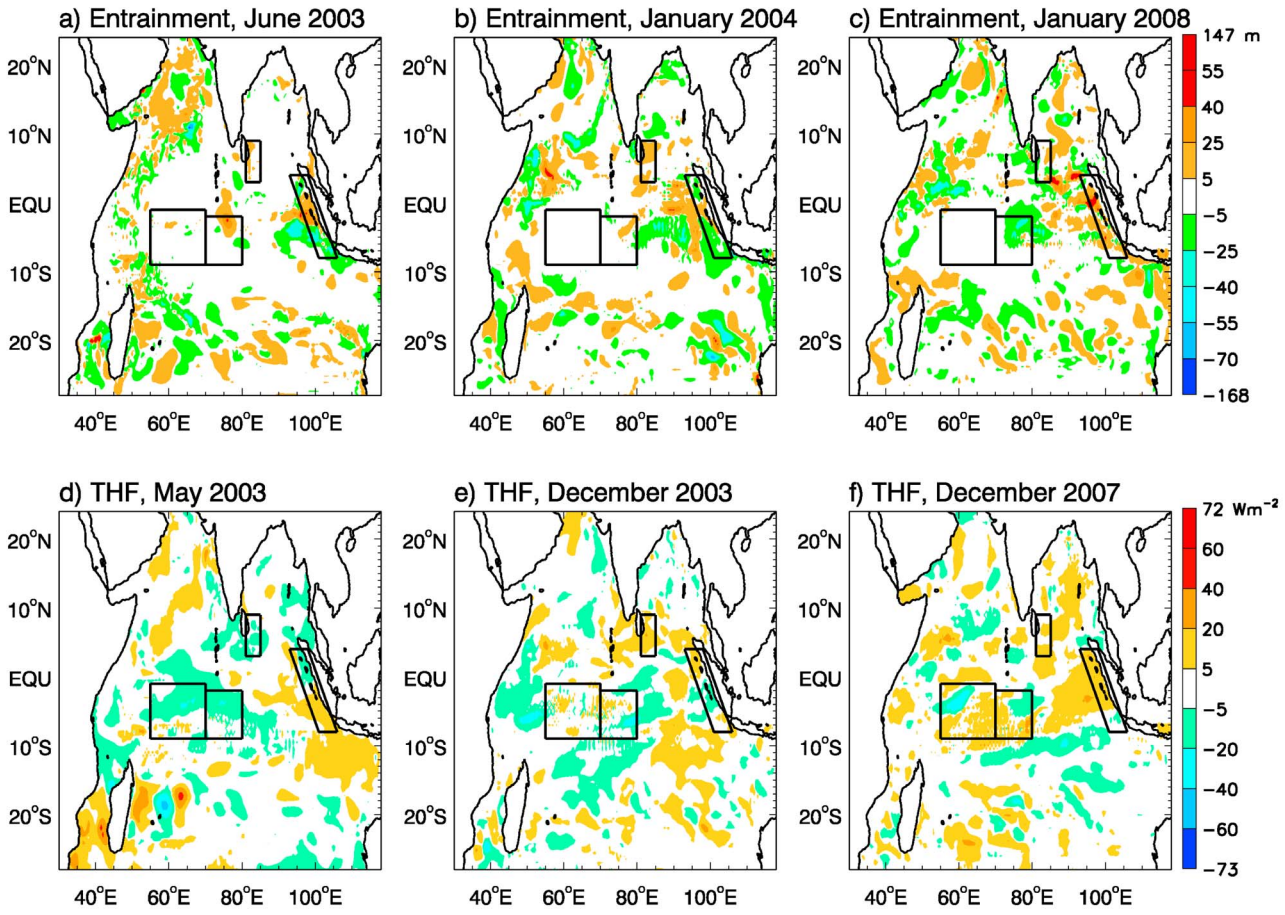

Figure 19. (a–c) Same as Figure 13, but for the interannual variability of hm due only to intraseasonal wind speed (HYCOM difference solution EXP3-EXP4). Boxed regions correspond to the SST representative regions of interest in Figure 15c. Units are m. (d–f) Same as Figures 19a–19c but for turbulent heat flux (THF). Units are Wm^{-2}.

vertical current shear due to intraseasonal wind stress play a much larger role than intraseasonal SW radiation and precipitation in causing seasonal-to-interannual rectification of atmospheric ISOs on SST, hm, and upper ocean heat content (Figures 9, 11, 12, 16, 17, and 18). However, the relative importance of wind speed and wind stress generally varies between signals, regions, and months. Exceptions to this are the rectified seasonal cycle of upper ocean heat content in all regions of interest (Figure 11), and the seasonal cycle of hm in the west equatorial IO (Figure 9f), all of which are consistently dominated by intraseasonal wind stress. In general, however, all five "wind" processes contribute in varying amounts to seasonal and interannual SST rectification from month to month, and from region to region.

[59] There is consistently strong atmospheric ISO rectification onto the seasonal cycle of SST in the Arabian Sea, the west equatorial IO, the southwest IO, and the BOB. The strongest rectification occurs in the AS and the BOB in April and May (Figure 12a). During these inter-monsoon months, the intraseasonally forced seasonal SST warms by 0.6°C, which can impact convection over the already warm Arabian Sea. The rectified SST signal is most strongly forced by intraseasonal wind speed (Figure 12d). Intraseasonal wind stress, precipitation, and SW radiation all play a reduced role (Figure 12a). During April and May in the Arabian Sea and the BOB, ISOs reduce the mean winds (Figures 10a–10c), causing reduced entrainment and increased THF due to reduced evaporation (Figure 13b and 13c), and resulting in consistently warmer SSTs (Figure 12a).

[60] The strongest ISO impacts on modeled interannual SST are found in the west, central, and east equatorial IO (Figure 15c). Generally, intraseasonal wind dominates intraseasonal SW radiation and precipitation, although the latter two processes contribute to interannual SST rectification during some months in some regions (Figure 18). Entrainment and THF due to intraseasonal wind speed and upwelling, horizontal advection, and mixing due to intraseasonal wind stress contribute in varying amounts to ISO rectification onto interannual SST.

[61] The regions with strong atmospheric ISO rectification onto the seasonal cycle and interannual variability of hm and upper ocean heat content are very similar (Figures 8a, 8b, 15a, and 15b). These similarities across timescales indicate that interannual hm and upper ocean heat content variability

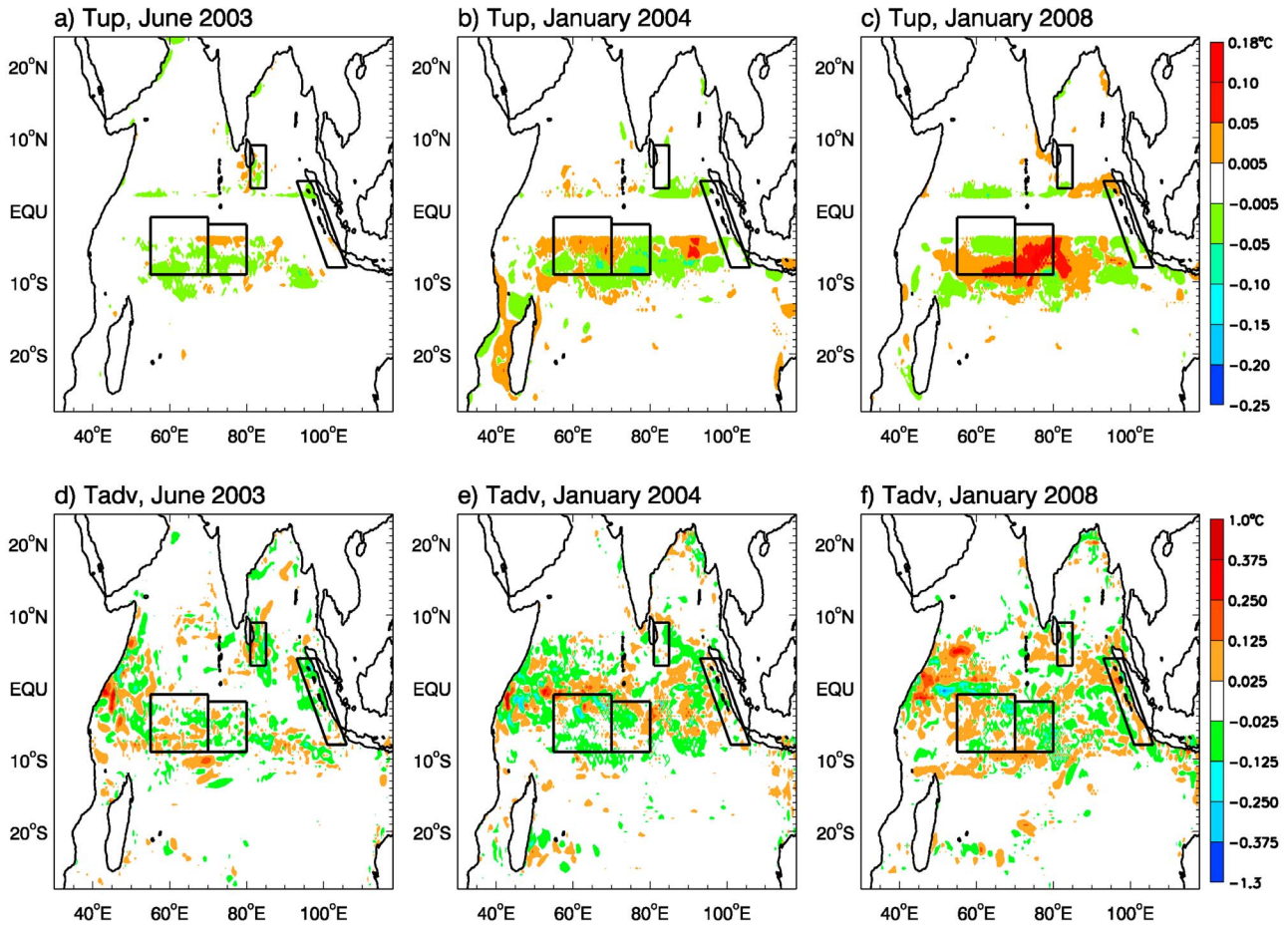

Figure 20. (a–c) Same as Figure 14, but for the interannual variability of Figures 20a–20c the change in SST (dT) due only to upwelling forced by intraseasonal wind stress. Boxed regions correspond to the SST representative regions of interest in Figure 15c. (d–f) Same as Figures 20a–20c but due only to horizontal advection forced by intraseasonal wind stress. Units are °C.

in these regions represents changes in the amplitude of the seasonal cycle of hm and upper ocean heat content from year to year.

[62] Our model results show that atmospheric ISOs can have an important impact on seasonal-to-interannual variability of the upper layers of the IO. This work presents a clean experimental design that can easily be reproduced using a range of models and forcing fields. Future work using coupled atmosphere-ocean models and a range of different forcing products could be used to confirm the robustness of our results. It would also be valuable to use similarly designed experiments to evaluate the impact of ISOs on known specific seasonal-to-interannual features like the Wyrtki Jet, the IO thermocline ridge, and the IOD.

[63] **Acknowledgments.** We thank ECMWF and NCAR for providing ERA-40 fields, the NOAA-CIRES Climate Diagnostics Center for CMAP precipitation fields, Yuanchong Zhang for the ISCCP flux data, and W. Timothy Liu for preparing the QuickSCAT wind fields. We acknowledge the NODC for making the WOA05 data available through the Internet. Thanks also go to W. G. Large, Lakshmi Kantha, Ralph Milliff, and Baylor Fox-Kemper for their valuable input. Finally, we thank Laurie Trenary and Jih-Wang Wang for graciously sharing HYCOM model output for experiment HYCOM_InternalEXP. This research is supported by NASA Ocean Vector Wind Science Team Award 1283568 and NSF CAREER OCE 0847605.

References

Bleck, R. (2002), An oceanic general circulation model framed in hybrid isopycnic-cartesian co-ordinates, *Ocean Modell.*, *4*(1), 55–88, doi:10.1016/S1463-5003(01)00012-9.

Boyer, T. P., et al. (2009), *World Ocean Database 2009*, *NOAA Atlas NESDIS*, vol. 66, edited by S. Levitus, 216 pp., U.S. Gov. Print. Off., Washington, D. C.

Chatterjee, P., and B. N. Goswami (2004), Structure, genesis and scale selection of the tropical quasi-biweekly mode, *Q. J. R. Meteorol. Soc.*, *130*(599), 1171–1194, doi:10.1256/qj.03.133.

Chen, T. C., and J. M. Chen (1993), The 10–20-day mode of the 1979 Indian monsoon - its relation with the time-variation of monsoon rainfall, *Mon. Weather Rev.*, *121*(9), 2465–2482, doi:10.1175/1520-0493(1993)121<2465:TDMOTI>2.0.CO;2.

Dee, D. P., et al. (2011), The ERA-Interim reanalysis: Configuration and performance of the data assimilation system, *Q. J. R. Meteorol. Soc.*, *137*, 553–597, doi:10.1002/qj.828.

Duchon, C. E. (1979), Lanczos filtering in one and 2 dimensions, *J. Appl. Meteorol.*, *18*(8), 1016–1022, doi:10.1175/1520-0450(1979)018<1016:LFIOAT>2.0.CO;2.

Duncan, B., and W. Q. Han (2009), Indian Ocean intraseasonal sea surface temperature variability during boreal summer: Madden-Julian Oscillation versus submonthly forcing and processes, *J. Geophys. Res.*, *114*, C05002, doi:10.1029/2008JC004958.

Duvel, J. P., and J. Vialard (2007), Indo-Pacific sea surface temperature perturbations associated with intraseasonal oscillations of tropical convection, *J. Clim.*, *20*(13), 3056–3082, doi:10.1175/JCLI4144.1.

Duvel, J. P., R. Roca, and J. Vialard (2004), Ocean mixed layer temperature variations induced by intraseasonal convective perturbations over the Indian Ocean, *J. Atmos. Sci.*, *61*(9), 1004–1023, doi:10.1175/1520-0469(2004)061<1004:OMLTVI>2.0.CO;2.

Emanuel, K. (2001), Contribution of tropical cyclones to meridional heat transport by the oceans, *J. Geophys. Res.*, *106*(D14), 14,771–14,781, doi:10.1029/2000JD900641.

Flatau, M., P. J. Flatau, P. Phoebus, and P. P. Niller (1997), The feedback between equatorial convection and local radiative and evaporative processes: The implications for intraseasonal oscillations, *J. Atmos. Sci.*, *54*(19), 2373–2386, doi:10.1175/1520-0469(1997)054<2373:TFBECA>2.0.CO;2.

Fu, X. H., B. Wang, T. Li, and J. P. McCreary (2003), Coupling between northward-propagating, intraseasonal oscillations and sea surface temperature in the Indian Ocean, *J. Atmos. Sci.*, *60*(15), 1733–1753, doi:10.1175/1520-0469(2003)060<1733:CBNIOA>2.0.CO;2.

Halkides, D. J., and T. Lee (2011), Mechanisms controlling seasonal mixed layer temperature and salinity in the southwestern tropical Indian Ocean, *Dyn. Atmos. Oceans*, *51*(3), 77–93, doi:10.1016/j.dynatmoce.2011.03.002.

Halkides, D. J., W. Q. Han, T. Lee, and Y. Masumoto (2007), Effects of sub-seasonal variability on seasonal-to-interannual Indian Ocean meridional heat transport, *Geophys. Res. Lett.*, *34*, L12605, doi:10.1029/2007GL030150.

Halliwell, G. R. (2004), Evaluation of vertical coordinate and vertical mixing algorithms in the HYbrid-Coordinate Ocean Model (HYCOM), *Ocean Modell.*, *7*(3–4), 285–322, doi:10.1016/j.ocemod.2003.10.002.

Han, W. Q. (2005), Origins and dynamics of the 90-day and 30–60-day variations in the equatorial Indian Ocean, *J. Phys. Oceanogr.*, *35*(5), 708–728, doi:10.1175/JPO2725.1.

Han, W. Q., D. M. Lawrence, and P. J. Webster (2001), Dynamical response of equatorial Indian Ocean to intraseasonal winds: Zonal flow, *Geophys. Res. Lett.*, *28*(22), 4215–4218, doi:10.1029/2001GL013701.

Han, W. Q., P. Webster, R. Lukas, P. Hacker, and A. X. Hu (2004), Impact of atmospheric intraseasonal variability in the Indian Ocean: Low-frequency rectification in equatorial surface current and transport, *J. Phys. Oceanogr.*, *34*(6), 1350–1372, doi:10.1175/1520-0485(2004)034<1350:IOAIVI>2.0.CO;2.

Han, W. Q., W. T. Liu, and J. L. Lin (2006a), Impact of atmospheric submonthly oscillations on sea surface temperature of the tropical Indian Ocean, *Geophys. Res. Lett.*, *33*, L03609, doi:10.1029/2005GL025082.

Han, W. Q., T. Shinoda, L. L. Fu, and J. P. McCreary (2006b), Impact of atmospheric intraseasonal oscillations on the Indian Ocean dipole during the 1990s, *J. Phys. Oceanogr.*, *36*(4), 670–690, doi:10.1175/JPO2892.1.

Han, W. Q., D. L. Yuan, W. T. Liu, and D. J. Halkides (2007), Intraseasonal variability of Indian Ocean sea surface temperature during boreal winter: Madden-Julian Oscillation versus submonthly forcing and processes, *J. Geophys. Res.*, *112*, C04001, doi:10.1029/2006JC003791.

Han, W. Q., P. J. Webster, J. L. Lin, W. T. Liu, R. Fu, D. L. Yuan, and A. X. Hu (2008), Dynamics of intraseasonal sea level and thermocline variability in the equatorial Atlantic during 2002–03, *J. Phys. Oceanogr.*, *38*(5), 945–967, doi:10.1175/2008JPO3854.1.

Harrison, D. E., and G. A. Vecchi (2001), January 1999 Indian Ocean cooling event, *Geophys. Res. Lett.*, *28*(19), 3717–3720, doi:10.1029/2001GL013506.

Hendon, H. H., C. Zhang, and J. D. Glick (1999), Interannual variation of the Madden-Julian Oscillation during austral summer, *J. Clim.*, *12*, 2538–2550, doi:10.1175/1520-0442(1999)012<2538:IVOTMJ>2.0.CO;2.

Hermes, J. C., and C. J. C. Reason (2008), Annual cycle of the South Indian Ocean (Seychelles-Chagos) thermocline ridge in a regional ocean model, *J. Geophys. Res.*, *113*, C04035, doi:10.1029/2007JC004363.

Inness, P. M., and J. M. Slingo (2003), Simulation of the Madden-Julian Oscillation in a coupled general circulation model. Part I: Comparison with observations and an atmosphere-only GCM, *J. Clim.*, *16*(3), 345–364, doi:10.1175/1520-0442(2003)016<0345:SOTMJO>2.0.CO;2.

Jayakumar, A., J. Vialard, M. Lengaigne, C. Gnanaseelan, J. P. McCreary, and P. Kumar (2011), Processes controlling the surface temperature signature of the Madden-Julian Oscillation in the thermocline ridge of the Indian Ocean, *Clim. Dyn.*, *37*(11–12), 2217–2234, doi:10.1007/s00382-010-0953-5.

Kara, A. B., P. A. Rochford, and H. E. Hurlburt (2000), Efficient and accurate bulk parameterizations of air-sea fluxes for use in general circulation models, *J. Atmos. Oceanic Technol.*, *17*(10), 1421–1438, doi:10.1175/1520-0426(2000)017<1421:EAABPO>2.0.CO;2.

Kara, A. B., A. J. Wallcraft, and H. E. Hurlburt (2005a), A new solar radiation penetration scheme for use in ocean mixed layer studies: An application to the Black Sea using a fine-resolution Hybrid Coordinate Ocean Model (HYCOM), *J. Phys. Oceanogr.*, *35*(1), 13–32, doi:10.1175/JPO2677.1.

Kara, A. B., A. J. Wallcraft, and H. E. Hurlburt (2005b), Sea surface temperature sensitivity to water turbidity from simulations of the turbid Black Sea using HYCOM, *J. Phys. Oceanogr.*, *35*(1), 33–54, doi:10.1175/JPO-2656.1.

Kemball-Cook, S., and B. Wang (2001), Equatorial waves and air-sea interaction in the boreal summer intraseasonal oscillation, *J. Clim.*, *14*(13), 2923–2942, doi:10.1175/1520-0442(2001)014<2923:EWAASI>2.0.CO;2.

Kemball-Cook, S., B. Wang, and X. H. Fu (2002), Simulation of the intraseasonal oscillation in the ECHAM-4 model: The impact of coupling with an ocean model, *J. Atmos. Sci.*, *59*, 1433–1453, doi:10.1175/1520-0469(2002)059<1433:SOTIOI>2.0.CO;2.

Kessler, W. S., and R. Kleeman (2000), Rectification of the Madden-Julian Oscillation into the ENSO cycle, *J. Clim.*, *13*(20), 3560–3575, doi:10.1175/1520-0442(2000)013<3560:ROTMJO>2.0.CO;2.

Kiladis, G. N., and M. Wheeler (1995), Horizontal and vertical structure of observed tropospheric equatorial Rossby waves, *J. Geophys. Res.*, *100*, 22,981–22,997, doi:10.1029/95JD02415.

Large, W. G. G., and P. R. Gent (1999), Validation of vertical mixing in an equatorial ocean model using large eddy simulations and observations, *J. Phys. Oceanogr.*, *29*(3), 449–464, doi:10.1175/1520-0485(1999)029<0449:VOVMIA>2.0.CO;2.

Large, W. G., J. C. McWilliams, and S. C. Doney (1994), Oceanic vertical mixing - a review and a model with a nonlocal boundary-layer parameterization, *Rev. Geophys.*, *32*(4), 363–403, doi:10.1029/94RG01872.

Large, W. G., G. Danabasoglu, S. C. Doney, and J. C. McWilliams (1997), Sensitivity to surface forcing and boundary layer mixing in a global ocean model: Annual-mean climatology, *J. Phys. Oceanogr.*, *27*(11), 2418–2447, doi:10.1175/1520-0485(1997)027<2418:STSFAB>2.0.CO;2.

Lau, K. M., and D. E. Waliser (2005), *Intraseasonal Variability in the Atmosphere-Ocean System*, Springer, New York.

Levitus, S., and T. P. Boyer (1994), *World Ocean Atlas 1994*, vol. 4, *Temperature*, *NOAA Atlas NESDIS*, vol. 4, 129 pp., NOAA, Silver Spring, Md.

Levitus, S., R. Burgett, and T. P. Boyer (1994), *World Ocean Atlas 1994*, vol. 3, *Salinity*, *NOAA Atlas NESDIS*, vol. 3, 111 pp., NOAA, Silver Spring, Md.

Li, T. M., and B. Wang (1994), The influence of sea-surface temperature on the tropical intraseasonal oscillation - A numerical study, *Mon. Weather Rev.*, *122*(10), 2349–2362, doi:10.1175/1520-0493(1994)122<2349:TIOSST>2.0.CO;2.

Madden, R. A., and P. R. Julian (1971), Detection of a 40–50 day oscillation in zonal wind in tropical Pacific, *J. Atmos. Sci.*, *28*(5), 702–708, doi:10.1175/1520-0469(1971)028<0702:DOADOI>2.0.CO;2.

Madden, R. A., and P. R. Julian (1972), Description of global-scale circulation cells in tropics with a 40–50 day period, *J. Atmos. Sci.*, *29*(6), 1109–1123, doi:10.1175/1520-0469(1972)029<1109:DOGSCC>2.0.CO;2.

Madden, R. A., and P. R. Julian (1994), Observations of the 40–50-day tropical oscillation - A review, *Mon. Weather Rev.*, *122*(5), 814–837, doi:10.1175/1520-0493(1994)122<0814:OOTDTO>2.0.CO;2.

Maloney, E., and A. Sobel (2004), Surface fluxes and ocean coupling in the tropical intraseasonal oscillation, *J. Clim.*, *17*(22), 4368–4386, doi:10.1175/JCLI-3212.1.

Marshall, A. G., O. Alves, and H. H. Hendon (2008), An enhanced moisture convergence evaporation feedback mechanism for MJO air-sea interaction, *J. Atmos. Sci.*, *65*, 970–986, doi:10.1175/2007JAS2313.1.

McCreary, J. P., P. K. Kundu, and R. L. Molinari (1993), A numerical investigation of dynamics, thermodynamics, and mixed-layer processes in the Indian Ocean, *Prog. Oceanogr.*, *31*(3), 181–244, doi:10.1016/0079-6611(93)90002-U.

McPhaden, M. J. (1999), Genesis and evolution of the 1997–98 El Nino, *Science*, *283*(5404), 950–954, doi:10.1126/science.283.5404.950.

Miyama, T., J. McCreary, T. Jensen, J. Loschnigg, S. Godfrey, and A. Ishida (2003), Structure and dynamics of the Indian-Ocean cross-equatorial cell, *Deep Sea Res., Part II*, *50*(12–13), 2023–2047, doi:10.1016/S0967-0645(03)00044-4.

Murakami, T., and M. Frydrych (1974), Preferred period of upper wind fluctuations during summer monsoon, *J. Atmos. Sci.*, *31*(6), 1549–1555, doi:10.1175/1520-0469(1974)031<1549:OTPPOU>2.0.CO;2.

Murtugudde, R., and A. J. Busalacchi (1998), Salinity effects in a tropical ocean model, *J. Geophys. Res.*, *103*, 3283–3300, doi:10.1029/97JC02438.

Murtugudde, R., J. P. McCreary, and A. J. Busalacchi (2000), Oceanic processes associated with anomalous events in the Indian Ocean with relevance to 1997–1998, *J. Geophys. Res.*, *105*(C2), 3295–3306, doi:10.1029/1999JC900294.

Nagura, M., and M. J. McPhaden (2012), The dynamics of wind-driven intraseasonal variability in the equatorial Indian Ocean, *J. Geophys. Res.*, *117*, C02001, doi:10.1029/2011JC007405.

Numaguti, A. (1995), Characteristics of 4–20-day-period disturbances observed in the equatorial Pacific during the TOGA COARE IOP, *J. Meteorol. Soc. Jpn.*, *73*(2B), 353–377.

Prasad, T. G., and P. J. Hogan (2007), Upper-ocean response to Hurricane Ivan in a 1/25 degrees nested Gulf of Mexico HYCOM, *J. Geophys. Res.*, *112*, C04013, doi:10.1029/2006JC003695.

Rao, S. A., and T. Yamagata (2004), Abrupt termination of Indian Ocean dipole events in response to intraseasonal disturbances, *Geophys. Res. Lett.*, *31*, L19306, doi:10.1029/2004GL020842.

Saji, N. H., B. N. Goswami, P. N. Vinayachandran, and T. Yamagata (1999), A dipole mode in the tropical Indian Ocean, *Nature*, *401*(6751), 360–363, doi:10.1038/43854.

Saji, N. H., S. P. Xie, and C. Y. Tam (2006), Satellite observations of intense intraseasonal cooling events in the tropical south Indian Ocean, *Geophys. Res. Lett.*, *33*, L14704, doi:10.1029/2006GL026525.

Schiller, A., and J. S. Godfrey (2003), Indian Ocean intraseasonal variability in an ocean general circulation model, *J. Clim.*, *16*(1), 21–39, doi:10.1175/1520-0442(2003)016<0021:IOIVIA>2.0.CO;2.

Schott, F., J. P. McCreary, and G. C. Johnson (2004), Shallow overturning circulations of the tropical-subtropical oceans, in *Earth's Climate: The Ocean-Atmosphere Interaction*, *Geophys. Monogr. Ser.*, vol. 147, edited by C. Wang, S.-P. Xie, and J. A. Carton, pp. 261–304, AGU, Washington, D. C., doi:10.1029/147GM15.

Schott, F. A., S. P. Xie, and J. P. McCreary (2009), Indian Ocean circulation and climate variability, *Rev. Geophys.*, *47*, RG1002, doi:10.1029/2007RG000245.

Senan, R. D., D. Sengupta, and B. N. Goswami (2003), Intraseasonal monsoon jets in the equatorial Indian Ocean, *Geophys. Res. Lett.*, *30*(14), 1750, doi:10.1029/2003GL017583.

Sengupta, D., B. N. Goswami, and R. Senan (2001), Coherent intraseasonal oscillations of ocean and atmosphere during the Asian summer monsoon, *Geophys. Res. Lett.*, *28*(21), 4127–4130, doi:10.1029/2001GL013587.

Shaji, C., C. Wang, G. R. Halliwell, and A. Wallcraft (2005), Simulation of tropical Pacific and Atlantic oceans using a Hybrid Coordinate Ocean Model, *Ocean Modell.*, *9*(3), 253–282, doi:10.1016/j.ocemod.2004.07.003.

Shinoda, T., and H. H. Hendon (2002), Rectified wind forcing and latent heat flux produced by the Madden-Julian Oscillation, *J. Clim.*, *15*, 3500–3508, doi:10.1175/1520-0442(2002)015<3500:RWFALH>2.0.CO;2.

Sriver, R. L., and M. Huber (2007), Observational evidence for an ocean heat pump induced by tropical cyclones, *Nature*, *447*(7144), 577–580, doi:10.1038/nature05785.

Stevenson, J. W., and P. P. Niiler (1983), Upper ocean heat budget during the Hawaii-to-Tahiti shuttle experiment, *J. Phys. Oceanogr.*, *13*(10), 1894–1907, doi:10.1175/1520-0485(1983)013<1894:UOHBDT>2.0.CO;2.

Takayabu, Y. N., T. Iguchi, M. Kachi, A. Shibata, and H. Kanzawa (1999), Abrupt termination of the 1997–98 El Nino in response to a Madden-Julian Oscillation, *Nature*, *402*(6759), 279–282, doi:10.1038/46254.

Tang, W., and W. T. Liu (1996), Objective interpolation of scatterometer winds, *JPL Publ. 96-19*, pp. 16, Jet Propulsion Lab., Pasadena, Calif.

Vialard, J., G. R. Foltz, M. J. McPhaden, D. P. Duvel, and C. D. Montegut (2008), Strong Indian Ocean sea surface temperature signals associated with the Madden-Julian Oscillation in late 2007 and early 2008, *Geophys. Res. Lett.*, *35*, L19608, doi:10.1029/2008GL035238.

Vinayachandran, P., and N. Saji (2008), Mechanisms of south Indian Ocean intraseasonal cooling, *Geophys. Res. Lett.*, *35*, L23607, doi:10.1029/2008GL035733.

Waliser, D. E., K. M. Lau, and J. H. Kim (1999), The influence of coupled sea surface temperatures on the Madden-Julian Oscillation: A model perturbation experiment, *J. Atmos. Sci.*, *56*(3), 333–358, doi:10.1175/1520-0469(1999)056<0333:TIOCSS>2.0.CO;2.

Waliser, D. E., R. Murtugudde, and L. E. Lucas (2003), Indo-Pacific Ocean response to atmospheric intraseasonal variability: 1. Austral summer and the Madden-Julian Oscillation, *J. Geophys. Res.*, *108*(C5), 3160, doi:10.1029/2002JC001620.

Waliser, D. E., R. Murtugudde, and L. E. Lucas (2004), Indo-Pacific Ocean response to atmospheric intraseasonal variability: 2. Boreal summer and the Intraseasonal Oscillation, *J. Geophys. Res.*, *109*, C03030, doi:10.1029/2003JC002002.

Wallcraft, A. J., E. J. Metzger, and S. N. Carroll (2009), Software design description for the HYbrid Coordinate Ocean Model (HYCOM) Version 2.2, *Tech. Rep. NRL/MR/7320-09-9166*, Nav. Res. Lab, Stennis Space Center, Miss.

Wang, B., and X. S. Xie (1997), A model for the boreal summer intraseasonal oscillation, *J. Atmos. Sci.*, *54*(1), 72–86, doi:10.1175/1520-0469(1997)054<0072:AMFTBS>2.0.CO;2.

Wang, B., and X. S. Xie (1998), Coupled modes of the warm pool climate system. Part 1: The role of air-sea interaction in maintaining Madden-Julian Oscillation, *J. Clim.*, *11*(8), 2116–2135, doi:10.1175/1520-0442-11.8.2116.

Wang, J.-W., W. Han, and R. L. Sriver (2012), Impact of tropical cyclones on the ocean heat budget in the Bay of Bengal during 1999: 1. Model configuration and evaluation, *J. Geophys. Res.*, *117*, C09020, doi:10.1029/2012JC008372.

Watterson, I. G., and J. Syktus (2007), The influence of air-sea interaction on the Madden-Julian Oscillation: The role of the seasonal mean state, *Clim. Dyn.*, *28*, 703–722, doi:10.1007/s00382-006-0206-9.

Webster, P. J., A. M. Moore, J. P. Loschnigg, and R. R. Leben (1999), Coupled ocean-atmosphere dynamics in the Indian Ocean during 1997–98, *Nature*, *401*(6751), 356–360, doi:10.1038/43848.

Webster, P. J., et al. (2002), The JASMINE pilot study, *Bull. Am. Meteorol. Soc.*, *83*(11), 1603–1630, doi:10.1175/BAMS-83-11-1603.

Wheeler, M., and G. N. Kiladis (1999), Convectively coupled equatorial waves: Analysis of clouds and temperature in the wavenumber-frequency domain, *J. Atmos. Sci.*, *56*(3), 374–399, doi:10.1175/1520-0469(1999)056<0374:CCEWAO>2.0.CO;2.

Wu, M.-L., S. Schubert, I.-S. Kang, and D. Waliser (2002), Forced and free intraseasonal variability over the South Asian monsoon region simulated by 10 AGCMs, *J. Clim.*, *15*, 2862–2880, doi:10.1175/1520-0442(2002)015<2862:FAFIVO>2.0.CO;2.

Xie, P. P., and P. A. Arkin (1996), Analyses of global monthly precipitation using gauge observations, satellite estimates, and numerical model predictions, *J. Clim.*, *9*(4), 840–858, doi:10.1175/1520-0442(1996)009<0840:AOGMPU>2.0.CO;2.

Xie, S.-P., H. Annamalai, F. Schott, and J. P. McCreary (2002), Structure and mechanisms of south Indian Ocean climate variability, *J. Clim.*, *15*, 864–878, doi:10.1175/1520-0442(2002)015<0864:SAMOSI>2.0.CO;2.

Yu, L. S., and M. M. Rienecker (2000), Indian Ocean warming of 1997–1998, *J. Geophys. Res.*, *105*(C7), 16,923–16,939, doi:10.1029/2000JC900068.

Zhang, C., and M. Dong (2004), Seasonality of the Madden-Julian Oscillation, *J. Clim.*, *17*, 3169–3180, doi:10.1175/1520-0442(2004)017<3169:SITMO>2.0.CO;2.

Zhang, C., M. Dong, S. Gualdi, H. H. Hendon, E. D. Maloney, A. Marshall, K. R. Sperber, and W. Wang (2006), Simulations of the Madden-Julian oscillation in four pairs of coupled and uncoupled global models, *Clim. Dyn.*, *27*, 573–592, doi:10.1007/s00382-006-0148-2.

Zhang, Y. C., W. B. Rossow, A. A. Lacis, V. Oinas, and M. I. Mishchenko (2004), Calculation of radiative fluxes from the surface to top of atmosphere based on ISCCP and other global data sets: Refinements of the radiative transfer model and the input data, *J. Geophys. Res.*, *109*, D19105, doi:10.1029/2003JD004457.